



LumosX: 3D Printed Anisotropic Light-Transfer

Qian Lu

Computer Science & Engineering
Texas A&M University
College Station, Texas, USA
qianlu@tamu.edu

Jacob Sayono

Mechanical and Aerospace
Engineering
University of California, Los Angeles
Los Angeles, California, USA
jacobsayono@g.ucla.edu

Xiaoying Yang

Electrical and Computer Engineering
University of California, Los Angeles
Los Angeles, California, USA
xiaoyingy@ucla.edu

Yang Zhang

Electrical and Computer Engineering
University of California, Los Angeles
Los Angeles, California, USA
yangzhang@ucla.edu

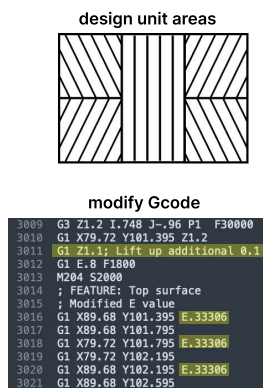
Xue Wang

Electrical and Computer Engineering
University of California, Los Angeles
Los Angeles, California, USA
xw526@ucla.edu

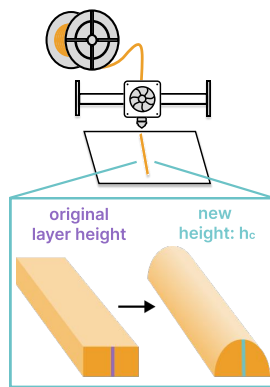
Jeeeun Kim

Computer Science & Engineering
Texas A&M University
College Station, Texas, USA
jeeeun.kim@tamu.edu

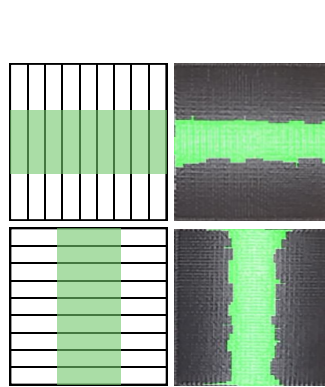
fabrication process



a linear sensing



b rotational/tilting sensing



c

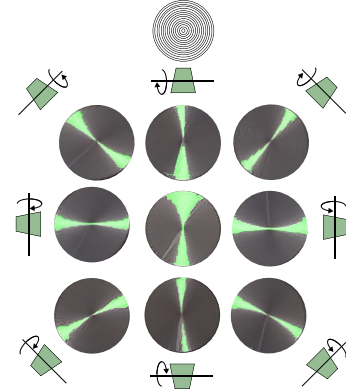


Figure 1: LumosX is a novel fabrication technique for encoding and decoding light signals that change with the viewer's position. It enables 3D-printed dynamic reflection patterns in FDM (a), which can appear on both flat surfaces for supporting linear sensing (b) and three-dimensional spaces for rotational/tilting sensing (c).

Abstract

Light's interaction with object surfaces through anisotropic reflection—where reflected light varies with viewing angles—offers significant potential for enhancing visual capabilities and assisting informed decision-making. Such ubiquitous light transfer phenomenon supports directional information encoding in sensing and dynamic display applications.

We present LumosX, a set of techniques for encoding and decoding information through light intensity changes using 3D-printed optical anisotropic properties. By optimizing directional reflection and brightness contrasts through off-the-shelf materials and precise control over processing parameters (e.g., extrusion volume, raster angles, layer height, nozzle positioning), we enable cost-effective

fabrication of visually enhanced objects. Our method supports modular assembly for highly curved regular surfaces and direct printing on top of relatively flat curved surfaces, enabling flexible information encoding for diverse applications. We showcase LumosX's effectiveness through various indoor and smart urban sensing scenarios, demonstrating significant improvements in both human interaction and autonomous machine perception.

CCS Concepts

- Hardware → Sensors and actuators; Sensor applications and deployments;
- Human-centered computing → Human computer interaction (HCI).

Keywords

3D printing, light transfer, sensing, dynamic information display

ACM Reference Format:

Qian Lu, Xiaoying Yang, Xue Wang, Jacob Sayono, Yang Zhang, and Jeeeun Kim. 2025. LumosX: 3D Printed Anisotropic Light-Transfer. In *CHI Conference on Human Factors in Computing Systems (CHI '25)*, April 26–May



This work is licensed under a Creative Commons Attribution 4.0 International License.
CHI '25, Yokohama, Japan

© 2025 Copyright held by the owner/author(s).
ACM ISBN 979-8-4007-1394-1/25/04
<https://doi.org/10.1145/3706598.3714124>

01, 2025, Yokohama, Japan. ACM, New York, NY, USA, 21 pages. https://doi.org/10.1145/3706598.3714124

1 Introduction

Light, as a unique carrier of the information signal for visual perception, has been widely used for sensing and displaying rich information indoors and outdoors. From signage to city-scale reflectors on road signs, urban inhabitants often rely on improved visual cues of critical information when making critical decisions. While today's 3D printing is inexpensive enough to create custom interactive devices that foster sensing and dynamic information display capabilities, most resulting artifacts are passive and need complicated electronics to respond to dynamic changes. Even with some techniques embedding visual markers into 3D-printed passive objects (e.g., G-ID [5], LayerCode [29], BrightMarker [6], etc.), the information displayed is often uni-directional allowing for one-time, situational captures only.

Anisotropic reflection is one optical phenomenon of anisotropy that exhibits different properties in varying directions depending on where it is viewed in our everyday life [9]. It is characterized by the direction-dependent appearance of surfaces under varying angles and lighting conditions, resulting from the inconsistent microstructure on the surface of objects. Anisotropy governs the varied direction in which light is reflected as common examples shown in hair, CDs, and brushed metal finish, highlighting the complex relationship between light and surface texture (Figure 2). Recognizing light, natural and artificial, as a stimulus for visual effects in numerous applications, we apply the unique properties of anisotropic effect in novel light-transfer applications.



Figure 2: Everyday examples of anisotropic reflection: (a) hair © StockCake, Public Domain, (b) CD © John Liu, CC BY 2.0, (c) door stop, (d) kettle © Marco Verch, CC BY 2.0 Germany, and (e) metal door handle © Jonathan Petersson, Pexels license.

The challenge lies in the microstructural scale that underpins anisotropic reflection—such as the fine grain in brushed metals. Creating anisotropic reflection remains challenging and costly for HCI researchers and potentially end-users without access to high-precision equipment to explore and utilize this phenomenon in developing various sensing applications at low cost. There is a noticeable gap, suggesting a need for easy and inexpensive solutions.

In response, we introduce *LumosX*, a fabrication technique to embed enhanced visual capabilities into passive 3D-printed objects, leveraging the anisotropic effects to transform light characteristics into a novel form of information transmission. We seek to extend the application front by embedding light-transfer capabilities into otherwise passive 3D-printed objects, enabling encoding and decoding of programmable information. *LumosX* can be used to develop interactive surfaces of 3D-printed objects with organic surface curvatures, where the visibility of information changes based on the

viewer's angle to enhance user engagement. Utilizing anisotropic reflection for signage allows for directional visibility, *LumosX* can replace 2D barcode alternating a series of binary digits to signify unique information about a product, be integrated into passive markers for state sensing and human activity sensing, directional cues for mobile domestic agents such as robot vacuum, and more. Our contribution is threefold:

- A characterization of 3D-printed anisotropic reflection to develop novel sensing principles and encoding information in 3D-printed objects by optimizing reflective capabilities.
- An information decoding principle, integrated into a mobile app to enable sensing using an inexpensive, standard smartphone RGB camera.
- Validation of 3D-printed anisotropic reflection through application scenarios and experimental testing.

2 Related Works

2.1 Fabricating Visual Cues

Lately, HCI research has investigated methods to enhance visual cues, such as detecting vital information using retro-reflective markers on a city scale [48], to help users make informed decision-making in various contexts. Examples include novel interface design to help drivers with ambient light displays were shown to help in navigation [30]. Point light movement is used for peripheral guidance [40], and lane change assistance is provided using traffic light colors and abstracted emotional faces [44]. Using a hybrid fabrication technique, electro-luminescent ink has been used to create interactive information displays [14, 39]. Paper-based LED interfaces have also been explored to provide feedback [24].

This body of work shows that the dynamic changes in perceptible properties of an interface can cater to smart capabilities in passive objects. However, existing techniques necessitate laborious steps for fabrication, often made separately to attach to the target objects. We utilize consumer-grade 3D printing as a promising solution to fabricate the global and local geometry to form a device from factors (shapes) as well as smart capabilities (functions).

2.2 3D Printing of Passive Visual Markers

With the latest advances in 3D printing technology, use of 3D printed passive artifacts to deliver dynamic visual capabilities became possible such as in lenticular objects which are viewpoint-dependent visual cues that can be provided [47], optical channels to route light signals internally through the 3D objects for display and acoustic sensing [42], adaptive information inking using photochromic pigments [23, 34], imprinting unique markers to identify and help manipulation of physical objects [26, 29], embedding hidden information within fabricated objects, leveraging Terahertz imaging for applications such as object identification, pose estimation, and data storage [43], and more.

Given a wider choice of advanced materials, off-the-shelf phosphorescent filament was brought to the 3D printing community's attention for visual expression using glow-in-the-dark effects in clocks and signs (e.g., Thingiverse glow-in-the-dark designs [32, 36, 41]), hiding marker information behind the special cameras such as IR camera by adopting infra-red reflection [7], and fluorescence [6].

	Invisibility	Non-flat Surfaces	All-in-one Fabrication	Fabrication	Information Decoding	Real-time Detection	Information Tagging	Dynamic Densing	Dynamic Display
Hou et al. [16]	+	✓	✓	FDM	3D scanner	✗	✓	✗	✗
Delmotte et al. [4]	+	✗	✓	FDM	Paper scanner	✗	✓	✗	✗
AirCode [26]	++	✗	✓	SLA or similar	Projector + camera	✗	✓	✓	✓
InfraStructs [43]	++	✗	✓	SLA or similar	Terahertz camera	✗	✓	✗	✗
Acoustic Voxels [25]	+/-	✓	✓	All	Acoustic device	✓	✓	✗	✗
Acoustic barcodes [15]	--	✗	✓	All	microphone	✓	✓	✗	✗
G-ID [5] (infill)	++	✗	✓	FDM	RGB camera	✗	✓	✗	✗
LayerCode [29] (color)	--	✓	✓	Dual color FDM	RGB camera	✗	✓	✗	✗
LayerCode (near-infrared)	++	✓	✓	Dual color SLA	Camera + NIR filter	✗	✓	✗	✗
AnisoTag [28]	+	✗	✓	FDM	Detection prototype	✓	✓	✗	✗
AnisoTag (camera) *	+	✗	✓	FDM	RGB camera	✗	✓	✗	✗
Lenticular Objects [47]	--	✓	✗	Multi color Polyjet	Naked eyes	✓	✓	✓	✓
BrightMarker [6]	++	✓	✓	Dual material FDM	NIR camera	✓	✓	✗	✗
LumosX	+	✓	✓	FDM	RGB camera	✓	✓	✓	✓

Figure 3: LumosX’s Value Proposition. The upper left part with bold borderlines is directly taken from AnisoTag [28]. Invisibility is evaluated based on how noticeable the artifacts are: ‘++’ indicates completely invisible to human naked eyes, ‘+’ indicates barely noticeable unless viewed closely, ‘+/-’ indicates noticeable at first glance, and ‘-’ indicates very obvious. Non-flat surfaces refers to the technique’s ability to support fabrication on regular or irregular curved surfaces, either through modular assembly or directly printing. The background color of fabrication and decoding devices reflects their availability and cost: green for common and affordable, pink for either uncommon but inexpensive or common but expensive, and red for rare or costly. Two recent relevant works and columns for tagging and dynamic sensing have also been added.

The most related work to ours is tackling similar approaches of using unique FDM printing taints given uni-material printing settings, to convey a changing visual appearance simply by adjusting 3D printing parameters only, through raster angles [5] or temperature changes in printing [33]. This work contributes to the existing track of research of a new 3D printing technique that makes the fabrication of passive 3D objects capable of displaying programmable information, leveraging common optical phenomena observed in our natural settings. Our work extends beyond static tagging and allows for dynamic, real-time sensing.

2.3 Information Display using on 3D Printed Anisotropy

Prior work has investigated imprinting light reflective information using 3D printing by delving into reflection characterization under different material properties [12, 22]. These works offer insights into light interaction with materials while falling short in incorporating it into human interaction sense.

Closest to our work is AnisoTag [28], which utilizes the anisotropic reflection pattern of printed line geometry, illuminated by a focused laser beam, to project the reflections from a 3D object’s surface onto another 2D surface to encode information. The key distinction between AnisoTag and our work lies in the encoding parameter: AnisoTag uses projection angle (θ) as the encoding parameter, while LumosX leverages light intensity changes, making decoding simpler and more accessible. This fundamental difference not only shapes the marker design and operational process but also drives completely different design strategies. For example, in our work, the dimensions of segmented unit areas play a critical role, as it involves whether the information is decoded using reflection orientation shifts or brightness contrasts (Section 6). In contrast, AnisoTag’s

design process is less influenced by unit area dimensions. Additionally, LumosX encodes and decodes in place, while AnisoTag projects illumination patterns on a secondary surface. AnisoTag relies on a precisely aligned focused laser beam, while LumosX responds to ambient lights. Table 1 summarizes key differences.

LumosX sets itself apart from existing works in several key ways. First, its unique ability to utilize highly reflective filaments and ambient light sources to encode information. Second, it detects such reflections using standard RGB cameras. Finally, LumosX encodes and decodes directly from 3D printed objects’ surfaces, without the need for a secondary screen and complex sensors (e.g., a series of photo-registers and voltage dividers), allowing for low-cost, battery-free approaches to enhance visual capabilities for sensing.

	AnisoTag	LumosX
Encoding Parameter	Projection angle θ	Light intensity
Reading & Decoding	Project to secondary surface	In-place
Light Source	Focus light (e.g., laser beam)	Ambient light / scattered light

Table 1: Comparison of key differences between AnisoTag [28] and LumosX

Building on the value proposition of AnisoTag [28], which compared similar works (bold borderlines), we extend LumosX beyond state-of-the-art techniques [4, 5, 15, 16, 25, 26, 29, 43, 47] (Figure 3). While prior works primarily focus on single-state tagging, our approach enables multi-state (bi-state and dynamic) information display and sensing. We support dynamic inputs such as moving

light sources, offer granular control over sensing parameters, and allow flexible encoding of information states. Additionally, we provide a composable library for converting motions between linear and rotational forms, enhancing sensing capabilities.

3 Background: Anisotropic Reflection

3.1 Specular Reflection

On smooth surfaces, such as mirrors, the incident light is reflected at the same angle as it hits the surface. Figure 4a illustrates a single ray of light, where the incident angle θ_i and reflection angle θ_r are equally divided by an imaginary line that is perpendicular to the surface normal. An object has many rays of incident light like this (Figure 4b). As we move further away from a smooth surface, the incident angle θ_i and reflection angle θ_r are getting smaller and smaller. When the viewpoint is infinitely far away, the incident and reflected rays become parallel to each other (Figure 4c), enabling the mirrored visibility of objects. Such a phenomenon is called specular reflection, or normal reflection.

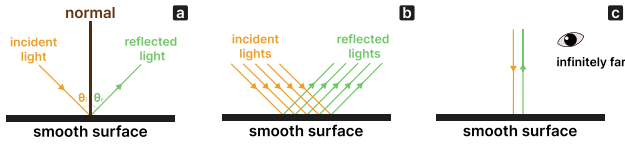


Figure 4: Specular (normal) reflection occurs when incident light bounces back at the same angle upon hitting a smooth surface (a), with multiple incident lights behaving similarly (b). When the viewpoint is far, the incident and reflected rays are parallel to each other (c).

3.2 Optical Anisotropy on Object Surface Texture

Reflection observed on a smooth surface follows the principles of specular reflection. However, when the surface microstructure introduces anisotropy, the behavior of reflected light can deviate from uniformity. The anisotropic effect of reflection refers to the direction-dependent appearance of certain materials or surface texture, as opposed to the isotropic effect which shows uniform appearance in all directions [9]. This phenomenon arises from the inconsistent microstructure of object surfaces, resulting in varied light reflection directions. It can be formally analyzed using the Bidirectional Reflectance Distribution Function (BRDF), which describes how light reflects based on incoming and outgoing directions. Anisotropic reflection can be observed in any object with fine grain aligned in one main direction as seen in Figure 2 of common examples.

By examining the inherent cylindrical shape of individual human hairs, we delve into the concept of anisotropy [27], embracing both right cylinders and elliptic cylinders. Figure 5a illustrates a central axis running through a cylinder and its bases, with an imaginary plate positioned orthogonal to this axis. As previously discussed, incident and reflected lights align parallel to each other when the viewpoint is infinitely far away. Therefore, the normal, which is the bisector of the incident and reflected light rays, is also

parallel. For this reason, in this illustration we omit the incident light and normal. The imaginary plate can thus be understood as composed of infinitely many normals. The orthogonal reflections at each point on the cylinder's surface within the plate create a comprehensive reflective pattern. Given the cylinder's surface hosts innumerable such points, it reflects back light in all directions within the plate. We can view a cylinder as it has infinitely many plates along its axis (Figure 5b). When multiple cylinders are aligned in the same direction and placed close together, their individual reflections merge into a larger reflective region [10]. This region extends perpendicular to the alignment direction, which, in the context of 3D-printed surfaces, corresponds to the printed line direction (Figure 5c).

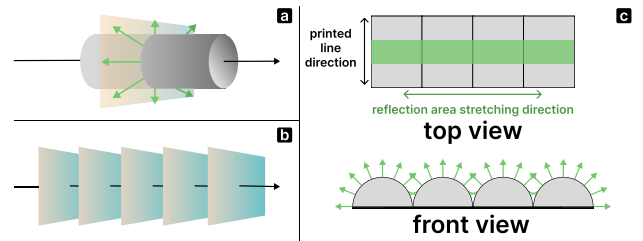


Figure 5: A cylinder reflects all reflections within a plate perpendicular to its axis (a) and can be thought of as having infinitely many such reflective planes (b). A surface covered with smooth half cylinders aligning in the same direction creates a long, stretched reflection region stretching perpendicular to the alignment direction (c).

3.3 Viewer Position And LumosX Reflection

The orientation of cylinders affects how light reflects and scatters in two primary directions relative to the viewer's position (Figure 6). 3D-printed lines oriented at 90° (vertical) to the observer create more regions of strong reflection, as light is scattered predominantly in directions perpendicular to the viewer's perspective. As a result, cylinders aligned at 0° (horizontal) appear relatively darker than those at 90°, producing a contrast in brightness.

4 Overview of LumosX

Our system mainly consists of three parts: encoding, fabrication, and decoding, as follows.

- **Encoding: LumosX Marker Design.** According to the desired information to encode and the usage scenarios, we determine the type of input and output—whether the marker should remain still (static or dynamic output) or the receiver (camera) should remain still (static or dynamic input) and the type of motion (linear or rotational) that should be associated with the design mechanism. Then we selected one of the two main design principles, (1) shift in reflection orientation or (2) contrast of brightness. Section 6 will detail the design principles.
- **Fabrication:** After the design is finalized for encoding, we implement the designs in FDM 3D printing by setting up

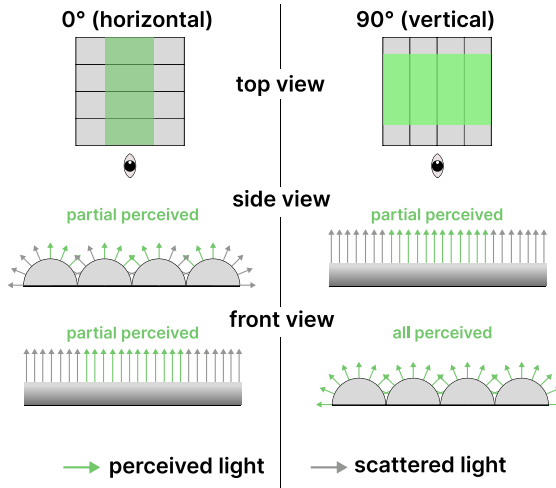


Figure 6: Top, side, and front views of cylinders arranged at 0° and 90° to the viewer’s position.

marker sizes, separating surface areas, and modifying printing parameters. After that, we construct the marker based on the type of motion and output a ready-to-be-attached mechanism.

- **Decoding: LumosX Marker Detection.** Upon receiving the dynamic light pattern, our algorithm decodes the information according to the series of light intensity changes associated with each unit area—either the reflected light intensity changes or the directions of high light intensity regions changes. In addition, our mobile app *LightIntensity*, a real-time light intensity measuring application, validates and helps visualize the information.

5 Example Application & Scenarios

We showcase our technique with a variety of applications and prototypes of their potential use scenarios, demonstrating the diverse sensing and information display capabilities enabled by LumosX in a real-world context. Figure 7 illustrates classification of LumosX capabilities based on the sensing and interaction types. State sensing refers to detecting a specific state at one point, activity sensing involves detecting ongoing activities, motion sensing focuses on detecting movement-related properties such as direction, speed, and displacement, and angle sensing deals with detecting angular positions or movements. The interaction is interpreted as (1) one-time outputs (e.g., reading metadata or state at a specific moment) or (2) continuous feedback or monitoring.

5.1 State Sensing

5.1.1 Embedding Metadata on 3D-Printed Barcode.

Following the general anisotropic reflection (Section 3.3) and principle to create contrast of brightness (Section 6.1.2), we can 3D print binary signal-based markers (e.g., barcode) with a single material. Unit areas with 90° raster angles (vertical) appear brighter, are embedding binary 0, and unit areas with 0° raster angles (horizontal) appear darker, thus representing binary 1.

Sensing Target			
	Activity	Motion	Angle
Information Display	Barcode (package) Barcode (smart appliance) Robot vacuum guide	Door/Window opening Tangible controllers	Room brightness control
	Pet feeder (consumption)	Door/Window opening Parking assistance Bike lane assistance	Room brightness control TV position adjustment Robotic perception
Monitoring/ Tracking			

Figure 7: Interaction scenarios classified by sensing types.

Figure 8a demonstrates a 3D-printed EAN-13 standard barcode that embeds 95 bits of information. Each bit is encoded in a 1mm width by 20mm height unit area (Figure 8d). Scan this barcode with any commercial scanner application, as depicted in Figure 8b, successfully retrieves the correct product information (Figure 8c).

Figure 9 illustrates barcode tagging on objects with non-planar surfaces and encoding information. This kind of information remains hidden during regular use but can be decoded when necessary. The tags and objects can be fabricated in one single step using the same material, eliminating the need for additional post-production process to attach tags. Additionally, compared to traditional paper-printed barcodes, these embedded tags are more durable and robust. Potential use cases include embedding security tags and hidden anti-counterfeiting information into plates of expensive jewelry collections (Figure 9a), ensuring authenticity and traceability. Similarly, tags can be applied to food packaging to encode supply chain data and certifications, enabling streamlined tracking of the transparency of food sources (Figure 9b). Another example is integrating pairing tags into home appliances like the smart coffee cup, which can pair with the coffee machine app to monitor coffee consumption, track drink temperature, or set reminders (Figure 9c).

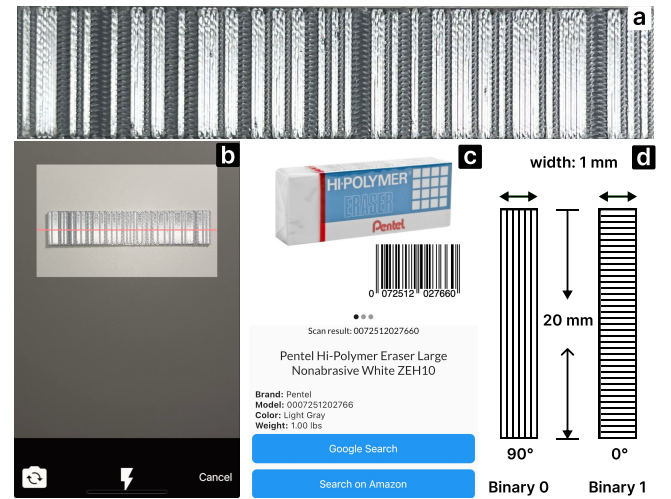


Figure 8: A 3D printed EAN-13 barcode containing 95 bits of information (a) with 1mm by 20mm dimension per bit (d). Scanning this barcode with any commercially available app (b) yields the correct product information (c).

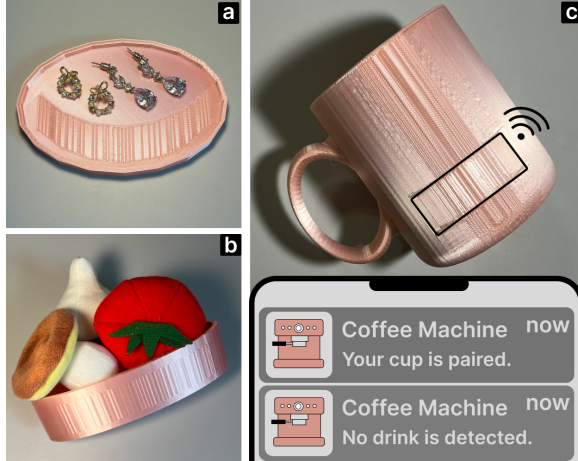


Figure 9: A jewelry plate with a barcode printed on its surface (a), a cylindrical food package (b) and a cup (c) with a barcode printed around their sides.

5.1.2 Container Fill Level Detecting. Containers like automatic pet feeders and vacuum robot dust bins operate with minimal human intervention, often leading to overlooked refilling or emptying needs due to infrequent maintenance. A container with contents tracking can be linked to various information of interest, both in short and long term, is designed using LumosX markers, which are composed of several unit areas with alternating raster angles, repeated based on the desired sensing granularity. By increasing the number of unit areas and adjusting their intervals, the system can achieve finer-grained sensing. In our example, the marker consists of ten unit areas (Figure 10a). When activated, the sensor remains still and turns on the flashlight to illuminate the mechanism. This allows the embedded system to detect the number of illuminated bars and calculate the container's fill level (Figure 10b and c).

Two real-world scenarios are developed here. An automatic pet feeder equipped with a LumosX marker (Figure 10b) only dispenses food when it detects the pet approaching. As shown in Figure 10d, when the sensor detects a low food level predefined by the users (e.g., 30%), it communicates with the central system, and the user receives a warning notification. Upon receiving the notification, the user can proceed to the shopping page of the preset cat food. As illustrated in Figure 10e, in situations where the pet owner is traveling and away from home, our system starts tracking the daily food consumption, compares it to the desired daily portion preset by the user, and generates daily reports. This is particularly useful for notifying the pet owner of any unusual eating behavior, and reminding them to take action, such as turning on the home security camera to check on their pet.

5.1.3 Symbolic Markers: Informative Perception for Mobile Agents. Traditional vacuum robots use infrared, ultrasonic, and lidar sensors for navigation [8], which is precise but costly. When the layout of a house changes, these robots must navigate the entire space and recreate the map, such a process can be time-consuming. Baseboards are naturally positioned along the edges of indoor environments, such as apartments and rooms, we can leverage this

placement to efficiently compute house mapping while maintaining accuracy. Our interactive baseboard offers a more affordable alternative using a camera-based mapping system. By sensing dynamic lighting patterns created by various raster angle alignments on surface unit areas, the robot, equipped with a camera, moves along the baseboard to scan LumosX markers and make its next decision, as shown in Figure 11. In this example, the markers encode two types of messages: (1) keep proceeding in the same direction, or (2) stop or change state.

Further designing the variety of markers to encode additional states can be a key direction for our future development. While currently optimized for indoor use, this sensing system can also be applied for broader applications in indoor navigation tools, including smart navigation aids for the visually impaired or obstacle avoidance in smart wheelchairs.

5.2 Activity Sensing: Dynamic Monitoring and Interaction

Smart systems often need a more granular interpretation of sensed information, such as dynamic state changes of movement or interaction. For instance, air quality monitors may adjust openings for optimal air exchange, balancing energy efficiency and security. Similarly, smart building management systems (BMS), noise control, and pet access systems can benefit from precise sensing and control over how much of doors or windows are open, minimizing the flow of heated or cooled air, keeping the home secure, and preventing wildlife trespassing.

LumosX activity sensing mechanism provides a cost-effective way for dynamic monitoring in various environments. We present three real-world scenarios: one for an indoor environment and two at a city scale. Our design features a sliding cover connected to the door or window via a composable linkage mechanism (Figure 12a-b) with a marker printed in alternating raster angles. As the door or window moves, the cover slides to expose more or less marker bars depending on the cover position. Analyzing the dynamic light pattern across the exposed marker sections allows for computing the degree of openness, with the sensing fidelity easily adjustable by modifying the number or spacing of the bars within the unit marker (Figure 12c). Applying this mechanism to a bedroom door can set the door to close tightly for privacy while leaving it open for pets to pass through. Similarly, parents can get a sense of the extent of windows opening and lock them in certain positions, allowing fresh air to flow while preventing children or pets from climbing out.

LumosX can easily expand its use cases to city-scale sensing. For cars that lack advanced radar sensors, parking assistance is a luxury. LumosX provides an adaptive alternative to anywhere it can be attached, parking poles or walls, to provide real-time proximity (Figure 12d). When activated by the car's lights during parking, a linear marker indicates how close the car is backing up. The user could be alerted using visual alarms or audio alerts. This real-time guidance enhances parking precision without requiring expensive upgrades to vehicles. Similarly, riding personal motor vehicles (e.g., bicycles, kick scooters, skateboards) in narrow bike lanes that are adjacent to motorways can be dangerous at night. Most do not have rear-view mirrors, making it difficult to observe approaching

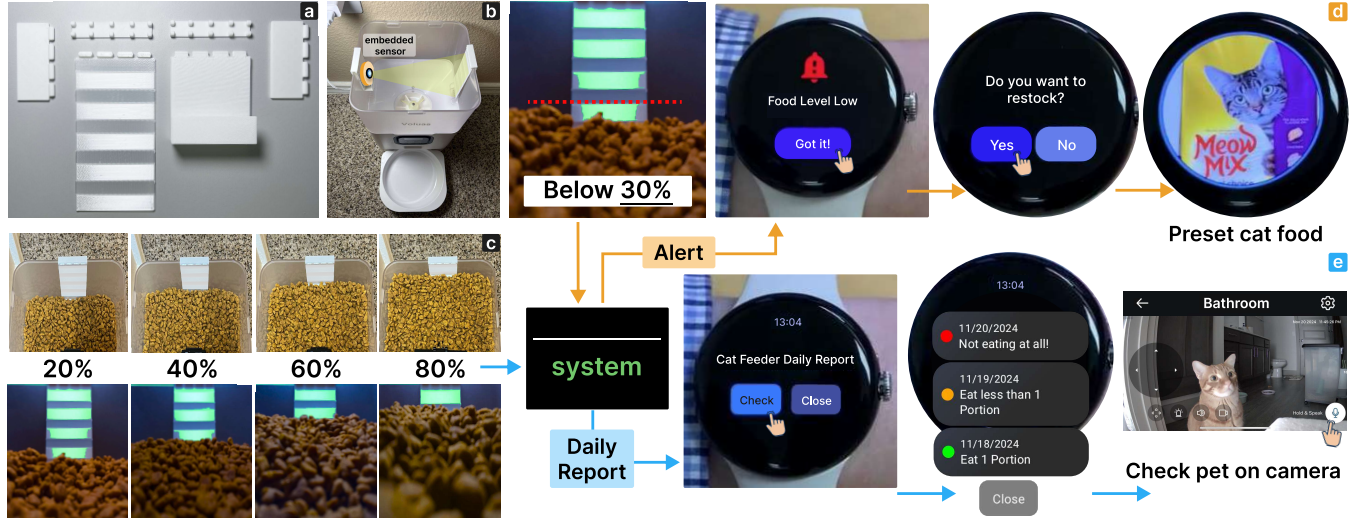


Figure 10: Composable components of the container detector (a) assembled and attached to an automatic pet feeder (b). The system accurately assesses the fill level of the feeder when activated (c). When the remaining food level is low, the system notifies the user, providing a direct link to the shopping page for restocking preset cat food (d). Additionally, when needed, the system tracks daily food consumption, compares it to the user-defined portion, and sends the daily report to the user, enabling them to monitor pet behavior and take actions such as checking on the pet via a camera (e).

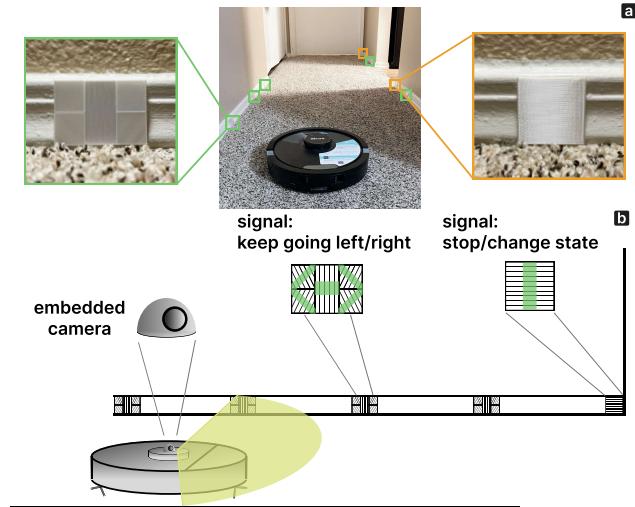


Figure 11: Real-life setup (a) and schematics (b) of the interactive baseboards.

vehicles from behind. LumosX markers attached to the bike lane are activated by approaching vehicles' headlights and can provide positional information. A user's personal device would send alerts based on the bicycle's distance. This improves situational awareness and ensures safer nighttime rides for users (Figure 12e).

5.3 Motion Sensing: Tangible Controllers

LumosX can be adapted to the rotational mechanism and sense motion direction, speed, and displacement. Figure 13a shows three

common physical controls, a rotational button, a push-down button, and a slider, where the cylinder rotation is triggered. We redesigned the rotation mechanism underneath to integrate a LumosX marker (see Figure 18a), where a flexible, soft belt structure wraps around the cylinder surface using snap-fit mechanisms (Figure 27a and c).

Two types of markers are used in the example: one with alternating raster angles to detect intermediate rotational displacement beyond basic start/end points (Figure 13c), and the second type detects rotational direction using two triangles separated by a diagonal line, with the upper having a 90° raster angle, while the lower has a 0°. As shown in Figure 13b, the lower triangle's green bars decrease its height while rotating clockwise, and the upper triangle reflects light horizontally. These markers embed information that can be applied to everyday objects for smart sensing applications, such as a smart temperature control system on cookware, where 60% hits the mark of a safe temperature to prevent burns or mold, as shown in prior work [45]. Figure 13d illustrates the scenario of a LumosX button being used to play the Flappy Bird game, where players control the bird's vertical motion through precisely timed inputs. The rotational direction, speed, and displacement of the cylinder component are accurately assessed to simulate the bird's movement. The tactile feedback provides players with a more immersive experience compared to traditional touchscreen input, enabling them to achieve greater precision in control.

5.4 Angle Sensing: Tilting Plate

For precise object angle sensing and positioning monitoring, using reflection patterns from circular print lines offers a cost-effective solution. A tilting plate stands on top of a ball joint, and allows for full degrees of freedom in movement. Figure 14a highlights how the LumosX marker's reflection changes with different tilting

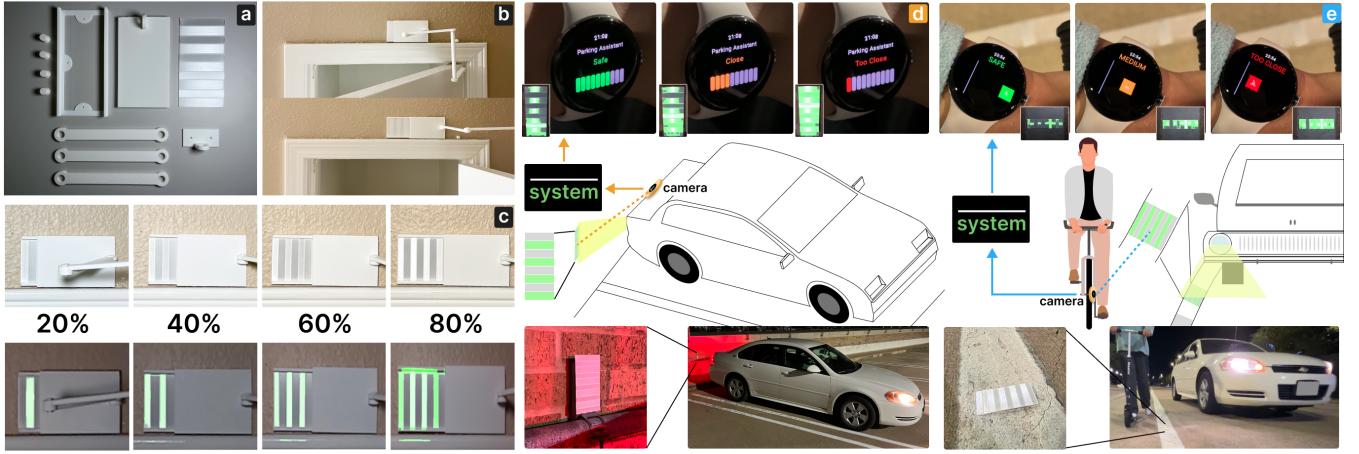


Figure 12: The door opening/closing detector assembled using composable blocks (a) to alter the motion types (b). Upon activation, not only the binary state (open/close) but also the level of the door opening can be assessed (c). Two real-world scenarios demonstrate the use of LumosX markers in city-scale. In the first scenario, the parking assistant system communicates with the marker and provides real-time distance evaluation, sending alarms to the user's smartwatch (d). In the second scenario, the bicycle riding assistant system is activated by the headlights of a passing vehicle. It communicates with the marker attached to the lane and provides real-time distance evaluation, sending arms to the user's smartwatch (e).

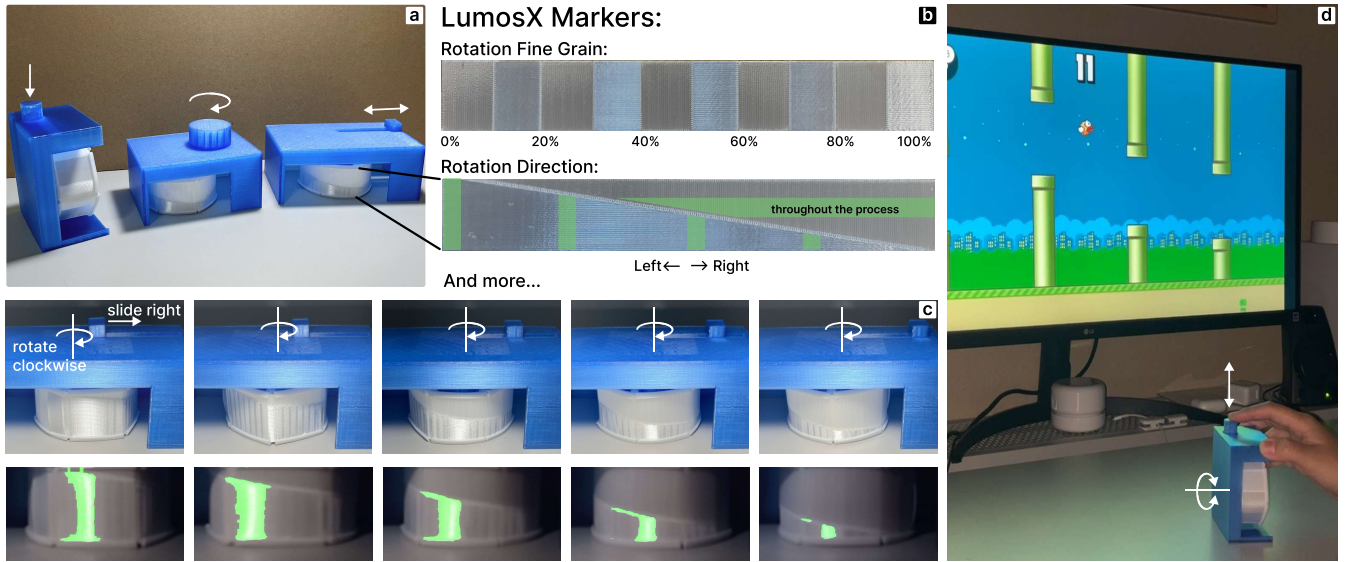


Figure 13: A button, rotation knob, and a slider (a), with the cylinder wrapped with LumosX markers (b). These markers are designed to sense motion direction speed. The example maker accurately assesses the rotation directions (c). Additionally, a LumosX button is demonstrated being used to play the Flappy Bird game (d).

angles, potentially useful for robotic manipulation (i.e., AirCode's robotic grasping task [26]). By reading the tilting plate attached to the bottle cap, the robotic arm can precisely determine the bottle's current position and orientation. This allows the robotic arm to execute tasks such as grasping the bottle with the correct alignment (Figure 14b).

Additionally, this design can be applied to human-centered smart home applications. For instance, the blind opening controller, as shown in Figure 15 a-d, enables dynamic adjustment of blinds to optimize room brightness. The pipeline begins with the user sending a command through a device (e.g., smartwatch) to "Make the room brighter." Upon receiving the command, the system communicates with the attached LumosX tilting plate to gather the current

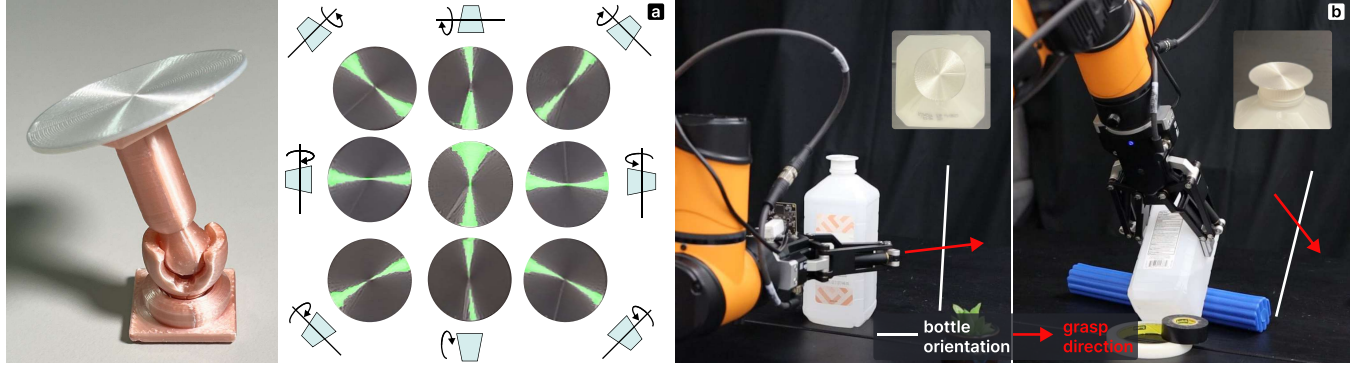


Figure 14: The tilting plate mounted on a rotational stand is viewed from various angles, with LumosXmarker featuring diagonal hourglass-shaped reflection regions corresponding to different tilting angles (a). A robotic arm knows the position to grasp a bottle by reading the tilting plate attached to the top of the bottle (b).

position of the blinds, while simultaneously collecting environmental lighting data. Using this information, the system computes the ideal adjustment (e.g., opening the blinds by 30°). The blinds then automatically adjust to this specified angle via the communication between the system and the LumosX tilting plate. Similarly, as illustrated in Figure 15 e-h, the tilting plate can be applied to adjust the TV position to eliminate glare on a TV screen caused by ambient light. The user initiates a command through a smartwatch, leading the system to analyze environmental factors and calculate the optimal rotational adjustment (e.g., 30° clockwise). Upon the communication between the system and the LumosX tilting plate, the TV stand rotates automatically to follow the adjustment.

6 LumosX Design and Processing: Techniques to Encode and Decode Information

In this section we present the three key components of our system: (1) designing LumosX marker to encode information, (2) capturing the encoded data, and (3) decoding the embedded information.

6.1 Encoding: Surface Segmentation for Directional Light

We use two general design strategies: (1) shifting reflection orientation and (2) adjusting brightness contrast.

6.1.1 Shift in Reflection Orientation. Anisotropic reflection informs that the brightest area stretches perpendicular to (crossing) surface line alignments, which is the underlying principle behind our project name, *LumosX* ("Lumos Cross"). Changing the line directions alters the reflection orientation, as seen in Figure 16a.

Dividing a surface into unit areas with alternating line directions creates dynamic reflections as the projected light source moves. The resulting shifts and patterns can be used to encode information. For example, counting the number of brighter bars can compute the precise states of doors or window opening degrees. Users can control granularity by adjusting unit area numbers and intervals. Additionally, strategic arrangements of unit areas can create meaningful reflection patterns, like in the vacuum robot guide example.

6.1.2 Contrast of Brightness. Aligning surface line orientations and dimensions, we can achieve uniform illumination across selected unit areas, creating a noticeable brightness contrast. We define the side of the reflection region perpendicular to surface lines as *LumosWidth* and the side parallel as *LumosHeight* (Figure 16a).

LumosHeight depends on light source distance and strength, increasing as the light source gets closer or brighter. Keeping the parallel dimension smaller than *LumosHeight*, the entire unit area will appear uniformly illuminated (Figure 16b). Users can apply this brightness contrast to applications such as barcodes and container detectors, where under a fixed light source, certain unit areas appear darker, while others appear brighter.

6.1.3 Special Case: Spiral Surface Lines. When the unit area is circular and filled with spiral lines, one can observe changes in both the orientation and dimensions of the reflection region. With the width of the reflection region (*LumosWidth*) consistently spans from the center to both ends, perpendicular to the spiral lines' orientation, an hourglass-shaped reflection is formed, which can rotate 360° (Figure 17a). The height of the reflection region (*LumosHeight*) and its orientation vary based on the viewing angle and the unit area's position (Figure 17b). Each side of the center displays a distinct *LumosHeight*, forming different sizes of reflection region. These dynamic reflection changes are more flexible than those with straight lines, enabling the detection of angle changes such as tilting and rotating.

6.1.4 Encoding Motions. The mechanical design allows linear information to be seen as rotational motion, enabling reading the motion profile, including rotational direction, speed, and displacement. Many common objects involve both motions, a typical example is the conventional slider. Figure 18 illustrates that our design can replace the underneath rotating cylinder of a slider (Figure 18b) with a thin LumosX marker wraps around (Figure 18a). When designing, users are recommended to consider what they aim to detect. Two examples are shown previously, one designed to track rotational displacement and the other to determine direction, both capable of reading speed (Figure 13b).

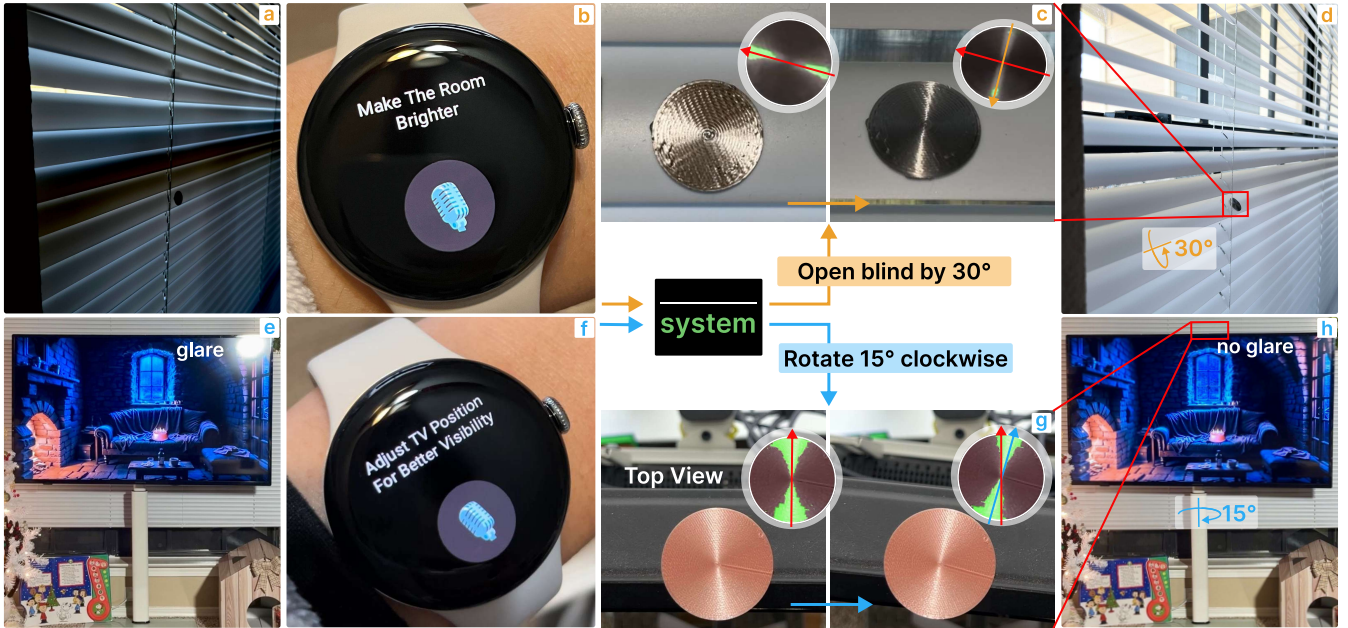


Figure 15: Two scenarios demonstrating the use of tilting plate in real-world context. In the first scenario, the room is too dark (a), and the user sends a voice command to the system to make the room brighter (b); the blind then communicates with the system via the attached tilting plate and executes the generated adjustment (c) to make the room brighter (d). In the second scenario, the TV has a glare on the screen (e), and the user sends a voice command to the system to fix the issue (f); the TV then communicates with the system via the attached tilting plate and follows the computed adjustment (g) to eliminate the glare (h).

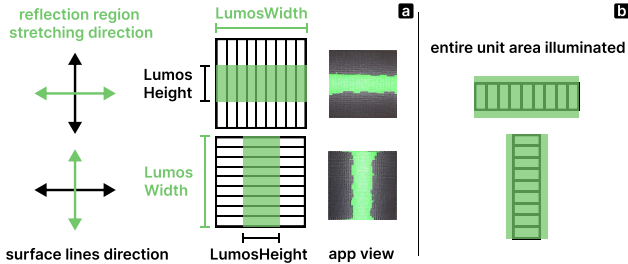


Figure 16: The long stretched reflection region extends in a direction perpendicular to the surface lines direction (a). Reducing the side parallel to the reflection height allows the entire unit area to appear illuminated (b).

6.2 Capturing: Real-Time Reading Using an RGB Camera

LumosX benefits from its compatibility with low-cost RGB cameras for context sensing, for which we utilize the contemporary OpenCV library to create a first-principle decoding algorithm. Mobile phones typically have a flashlight and camera on the back, making them readily available as light emitters and receivers. We developed *LightIntensity* to capture and interpret light intensity in real time. The app enables users to select a region of interest (ROI) (i.e., 15 by 15 red bounding box in Figure 19a), calculates the light intensity within ROI, and displays light intensity changes over

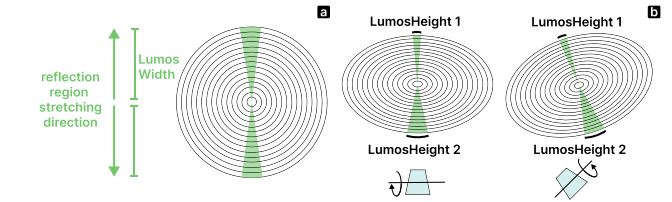


Figure 17: Unit areas with circular print lines produce hourglass-shaped reflection regions (a). The reflection height and orientation change depending on the viewing angle and unit area position (b).

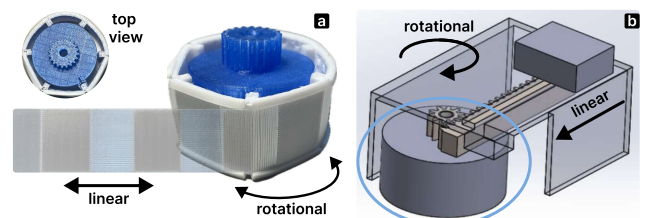


Figure 18: A LumosX marker designed for linear scanning is now wrapped around a rotational base (a), functioning as the cylinder mechanism of a conventional slider (b), enabling the transformation from linear to rotational motion.

time. To accommodate dynamic light changes in different environments, the app's other version, *idTag*, features adaptive thresholds that highlight areas of highest contrast (i.e., green bars versus dark areas) by identifying the range of light intensity within ROI (Figure 19b-c). The app is open-sourced and available for downloading via the LightIntensity repository¹ and the *idTag* repository².

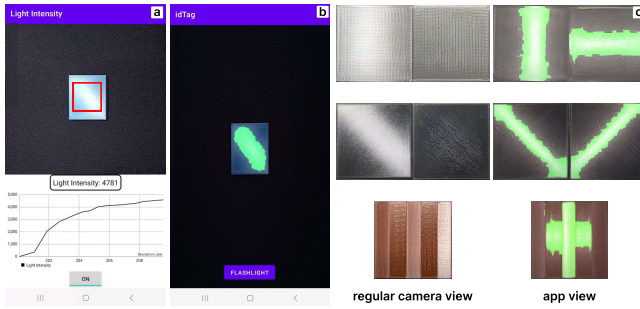


Figure 19: A 3D-printed panel under the *LightIntensity* app showing the average light intensity within the red bounding box (a) and another version of this app, *idTag*, highlighting detected reflection regions in green pixels (b). A comparison between panels under regular camera views and the app's view is shown in (c).

6.3 Decoding: General Markers

The algorithm begins by processing the RGB image of the encoded region captured by a camera using OpenCV's *Perspective Transform* to correct perspective distortions caused by perspective shifts. The region is then barbared by setting a threshold to separate bright (1's) and dark (0's) pixels. By analyzing the clusters of brighter pixels (reflection regions), the algorithm identifies the most prominent discontinuities, which mark the boundaries of unit areas.

For markers designed with reflection orientation shift, the algorithm detects changes in the dimensions of 1's pixel clusters between adjacent unit areas. Horizontal orientations are identified when brighter pixels form compact bands, while vertical orientations are seen by vertical clusters. Similarly, diagonal orientations (e.g., left-diagonal) are recognized when clusters are lined at specific angles, computing the sequence of reflection orientation shifts.

For markers designed with brightness contrast, we count the number of 1's within each unit area to label it as dark or bright. For complex cases like the LumosX barcode, where a single unit may encode multiple bits (e.g., "0000"), the algorithm identifies bit boundaries instead of unit boundaries by computing the gradient to determine bit edges. Following EAN-13 encoding [2], the first and last three bins of the barcode are used to estimate bit width. Pixels across these six bits are averaged to generate a binary sequence of 0's and 1's representing the barcode. This binary sequence is then decoded into a standard barcode string using EAN-13 principles.

¹<https://github.com/jacobsayono/lightintensityapp>

²<https://github.com/jacobsayono/id-tag>

6.4 Decoding: Angle of Tilting Plate

To sense rotation and tilting, we use the position of the reflection region and the geometric properties of the tilting plate (i.e., a perfect circle). First, we detect the plate's center and radius using OpenCV's *Hough Circle Transformation* (see Figure 20a). Within the detected area, we grayscale the sub-image and identify the brightest 1% pixels induced by anisotropic reflections. Next, we assign angels to the tilting plate (see Figure 20b) and fit the marked pixels with a first-degree polynomial, the azimuth angle ϕ is then computed from the slope of the fitted line. The polar angle θ is inferred from the plate's perspective distortion—as the plate tilts, it appears more elliptical. We calculate the angle by analyzing the ratio of the ellipse's minor axis (corresponding to *LumosWidth*) to its major axis.

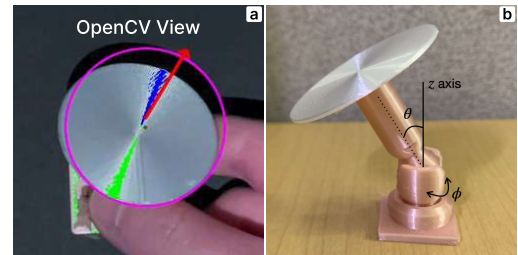


Figure 20: The OpenCV view of a tilting plate (a), which has two angles parameters θ and ϕ (b).

7 Fabricating LumosX Markers

The general process for fabricating LumosX markers in FDM 3D printing is: (1) segmenting the unit areas using CAD software, (2) configuring raster angles and other key parameters in a slicer tool, and (3) modifying the *.gcode* file.

7.1 Marker Construction

To help designers easily utilize our technique, we developed a *Blender* plugin³ for print file generation. The plugin supports three marker types: "Barcode," "Spiral," and "Grid," corresponding to barcode markers, tilting plates, and regular markers with grid structures, respectively (Figure 21).

7.1.1 Marker Dimension. Users can customize the marker dimensions within the plugin. The size of unit areas is typically constrained by the object being attached or the bed size of a 3D printer. For cases where unit areas need to be printed at smaller scales, such as barcodes, users should consider the scanning distance and printer precision. For example, barcodes scanned from a distance of 30cm require a reflection region height of at least 16mm, based on tests with a 180lux light source. To find out the minimum printed unit area width while retaining detail, we tested from 5mm and down to 0.5mm and found that a 1mm width by 20mm region per bit is the smallest printable size using a Bambu Lab P1P 3D printer.

³https://github.com/emoryluqian/LumosX_Marker_Generator

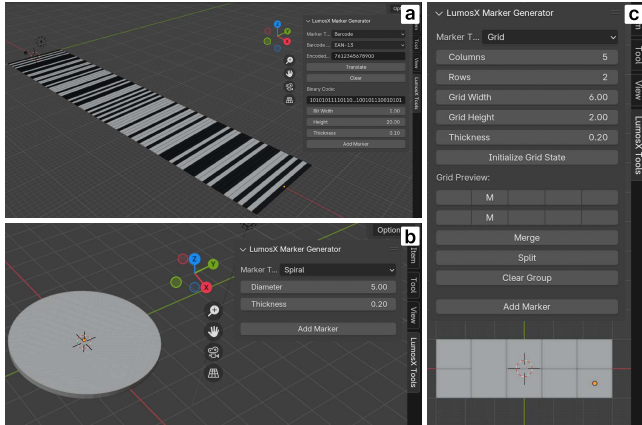


Figure 21: The *Blender* plugin that supports basic modeling or three types of markers: barcode (a), tilting plate (b), and regular markers with grid structures (c).

7.1.2 Marker Content.

- After choosing a marker type, users define:
- **Barcode** (Figure 21a): the plugin uses the "EAN-13" barcode type by default. Users simply input the encoded information, click "Translate," and the plugin generates the binary code sequence automatically.
 - **Spiral** (Figure 21b): No additional input is required. The plugin creates a circular plate for the tilting plate.
 - **Grid** (Figure 21c): Users can set the number of columns and rows to divide the marker into equal-sized unit areas. The "Grid Preview" allows users to merge or split cells using the "Merge" and "Split" buttons, enabling the encoding of specific information within cells.

Once all settings are finalized, clicking "Add Marker" generates the model files, organized into groups. For instance, in "Barcode" mode, files are grouped by binary values 0s and 1s, while in "Grid" mode, files are grouped by merged cells.

7.1.3 Export Model Files. Markers are exported as separate model files, not as a single file. Notice that if embedding a marker onto an object, users should first import the object's 3D file, align the marker, and export each group separately, including the model file with updated position and orientation data. In the future, we plan to enhance this toll by incorporating parameter optimization features.

7.2 Optimizing Anisotropy in FDM

Slicer software (e.g., Slic3r, Cura) outputs Gcode to guide FDM 3D printers in layer-by-layer fabrication. As the filament is fed into a heated nozzle, it melts and is extruded to form lines (Figure 22). Our focus is on adjusting nozzle position (X [mm], Y [mm]), height (Z [mm]), and extrusion amount (E [mm]) to control surface textures. In this section, we present the configuration of anisotropy in FDM and show how to program it through printer processing parameters.

7.2.1 Slicing Raster Angles: After exporting the model files, users should import them into slicer software to assign top surface raster angles. Recall that the reflection region stretches perpendicular to the surface line alignment, so the raster angle must differ by 90°

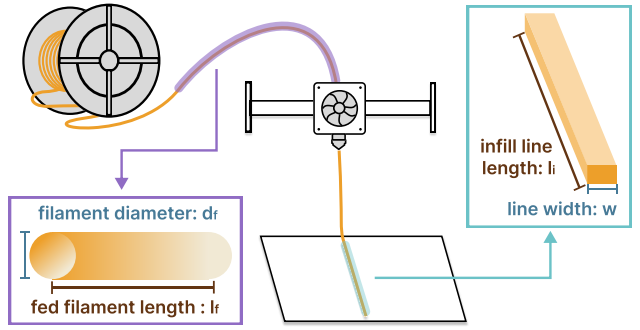


Figure 22: In conventional FDM 3D printing with regular slicer settings, the filament is fed into a heated nozzle, melted, and extruded as one line on the print bed.

from the intended reflection direction. For example, if horizontal (0°) reflection is desired, the rater angle should be set to vertical (90°). For markers designed with a shift in reflection orientations, the most noticeable effect occurs with a 90° angle difference between two adjacent unit areas. For markers designed with a brightness contrast, brighter areas should be set to 90° , while darker areas should be set to 0° , as discussed in Section 3.3.

7.2.2 Modify Surface Texture. Compared to a flat surface, a curved surface scatters ambient light more effectively due to increased reflection from varied angles. In FDM 3D printing, each layer typically contains flat lines with rectangular cross-sections. To enhance anisotropic reflection, we aimed to shape these lines into smoother, rounder shapes, maximizing surface normals across 180 degrees and reflection angles within 360 degrees [27]. To achieve this, we adjusted the print speed, line geometry, and nozzle position.

7.2.3 Adjusting Print Speed: After experiments, a print speed of 20–50mm/s is recommended for achieving the best smoothness across most filaments. When the speed falls outside this range, the printed line loses the desired smoothness, resulting in a rougher print and reducing the effect of anisotropic reflection.

7.2.4 Computing Surface Lines Geometry to Maximize Reflection: We aimed to create lines with a nearly spherical cross-section on the top surface while keeping the base flat for stability and strong adhesion on the underlying layers, resulting in a semicircular profile that optimizes reflection angles. To achieve this, the height (Z [mm]) value needs to be adjusted to match the desired spherical radius. Based on prior work [37], the filament volume fed into the nozzle must equal the volume extruded, which is calculated as the cross-section area multiplied by line length, as illustrated in Figure 22. Since we only alter the cross-section, the extrusion amount (E [mm]) in the Gcode must also be adjusted.

Following the method outlined in Ma's work [28], the E value can be computed as $E = c \times \frac{h_c \times w}{(d_f)^2} l_i$, where h_c is the adjusted height by lifting the nozzle (mm), w is the printed line width (mm), d_f is the diameter of fed filament (mm), l_i is the cross-section area (mm^2), and c is the coefficient (empirically set between 0.8–0.9) to prevent

compression while preserving the surface tension of printed lines. Appendix A details the step-by-step computation.

A comparison of standard flat lines and our modified semicircular lines, taken using the TOMLOV DM1 Wireless digital microscope (1000X magnification, 1080P resolution), signifies the differences in reflectivity (Figure 23). The infill lines with optimized geometry is superior with its reflectivity.

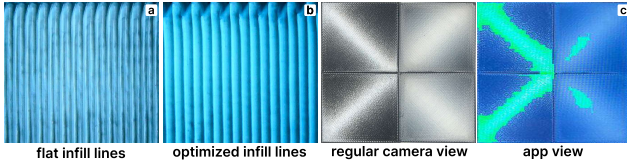


Figure 23: Microscope view comparing printed lines with a flat and squished appearance (a) versus a round and smooth shape (b). Both the regular camera view and *LightIntensity* app view show that directional light is more clearly defined on the surface with round and smooth lines (left half) than on the surface with standard flat lines (right half) (c).

Note that for accurate computation within the slicer, “*M83 relative extrusion mode*” must be activated, which generates E values for different mechanisms. This mode adjusts the extrusion amount of each line independently, without being impacted by previous extrusion or impacting others following.

Uniform Line Length: For unit areas with uniform line lengths such as rectangles with raster angles that are either parallel or orthogonal to the unit region shape, we can set a desired line lifting offset by adjusting the nozzle height from where the previous layer has been completed, corresponding to the Z command in Gcode. Note that this is different from the layer height setting in the slicer. For instance, if the layer height is set to 0.2mm, we set new height lines in the top layer to 0.3mm, then in Gcode, the Z value for the top layer should be increased by $0.3 - 0.2 = 0.1$. E values obtained from the above computation can replace the old values in Gcode to generate readily printable files.

Varying Fill Line Length: Another case is when the top surface comprises several unit areas with varying line lengths, such as a square panel with 45-degree raster angle surface lines and a circular panel with spiral surface lines as demonstrated in Figure 24b left. In such scenarios, the E value must be recomputed for each line, which would be impractical. Instead, computing a new height based on the existing E value determined by the slicer software can still achieve the desired shape. Rearrange the formula for computing the final E value above, the new height can be computed by

$$h_c = \frac{E \times (d_f)^2}{l_i \times w \times c} \quad (1)$$

, where $\frac{(d_f)^2}{wc}$ and the ratio of E value to length, $\frac{E}{l_i}$, remain consistent across different lines. Locating the top layer in the G-code and adjusting the Z value to reflect the new height. For example, with a default layer height of 0.2mm and a computed half-cylinder height h_c of 0.25mm, when printing the top layer with half-cylinder shaped lines, the nozzle lift offset is 0.05mm to meet the new height, by increasing the Z value by 0.05.

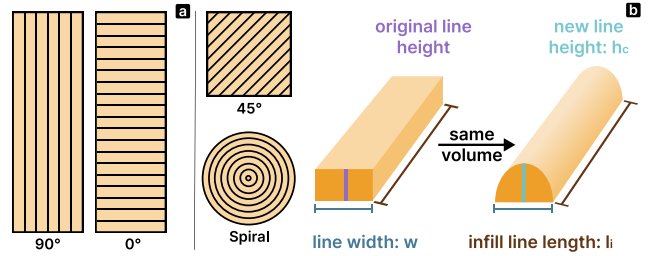


Figure 24: Surface unit areas containing uniform-length lines (a) and surface unit areas with varying-length lines (b).

7.3 Exploring 3D Printing on Non-Planar Surfaces

This section explores methods for embedding anisotropy on non-planar surfaces. One approach involves printing thin markers and use our snap fit design to wrap them around objects (see Section 5.3 slider control for example). Here we recommend a marker thickness of 0.1-0.2mm for easy wrapping. Another approach attempts direct printing on organic shapes, requiring z-hops within the same layer to accommodate sloped movements in FDM printers. However, due to the layer-by-layer nature of FDM 3D printing, smooth, continuous surfaces are often segmented into multiple layers that disable preserving correct raster angles. In many cases, a single unit area is sliced into multiple layers, leading to discontinued lines that cut smooth reflection patterns.

7.3.1 Constructing Marker Region for Separate Print Setting. Printing barcodes on non-planar surfaces needs two additional steps beyond the procedure for flat surfaces as shown in Figure 25a. First, set the barcode height enough to cover the curve of the target object surface before segmentation and grouping into 0s and 1s. This ensures the unit area width remains consistent when scanned from above (parallel to the normal) as it is projected flat, thus preserving equally sized bits and reading accuracy. Second, subtract the target object’s geometry to create a layer with the desired thickness that fits the object’s surface before exporting model files.

7.3.2 Modifying Nozzle Paths. To guide the nozzle along the slopes of curved surfaces in each unit area, we approximate the surface using tangent planes and adjust the Gcode accordingly. To do this, we need to locate the surface coordinates (X [mm], Y [mm], Z [mm]). The slider’s Gcode preview provides the coordinates of the edges of each unit area, which are used to approximate a flat tangent plane. Sometimes, multiple tangent planes will be needed as a unit area can be further segmented into smaller regions. Barcodes are printed with regions with lines either parallel or perpendicular to its height to present 0 and 1 bits respectively. Figure 25b-d presents two scenarios:

- **Figure 25b:** Lines adjust Z-coordinates dynamically along the slope in one stroke. After each line, the nozzle moves back to the next (X, Y) coordinate while recovering the previous Z-height, and continues to fill the unit area. The E value must be adjusted since the printed line would be longer than it is printed on a flat surface.

- **Figure 25c:** Lines remain at a fixed Z-height within each stroke but adjust between strokes to follow the slope.

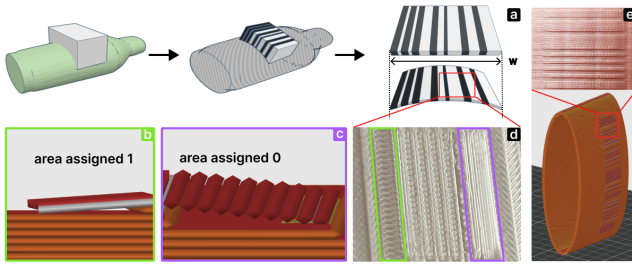


Figure 25: We obtain a surface geometry where barcode regions are warped on top, and unit areas are divided with desired raster angles for encoding bits (a). Then we use tangent plane approximation to compute z-hops alongside the slope in the unit area (b-d). Changing the printing position allows unit areas to be printed parallel to the print plate, and takes advantage of the smooth outer walls (e).

This method is still experimental, as there is no automated way to generate these coordinates for the entire marker. For now, coordinates must be manually adjusted, and we demonstrate this method with only two unit areas as a proof of concept (Figure 25d).

7.3.3 Printing Position Approach. For relatively flat curved surfaces, such as the bottle of a wine bottle, it's possible to encode binary with brightness contrast. Regions encoded as binary 0 (brighter) are aligned parallel to the object's layers, while regions less visible due to weaker reflections are seen as binary 1. FDM 3D printers create objects layer by layer, with surface lines aligned parallel to the printing plate. This property enables a possible approach of encoding binary 0s through specific printing orientations. As shown in Figure 25e, after embedding the 0's in object, the model is rotated 90 degrees, so it prints at a 0-degree raster angle. By slightly moving the nozzle outward, the binary 0 areas have more pronounced, reflective surface lines, making them appear brighter, while relatively darker regions are decoded as binary 1s. This method demonstrates a potential way to embed barcodes using brightness contrast, but it is still limited to relatively flat curved and simple geometries.

7.4 Material/Color Choices

We evaluated six commercially available reflective filaments for related reflection intensity. We first selected Reflect-o-Lay PLA [20], as it contains retro-reflective particles. Then we picked Hello3D Silver Glitter PLA [35] and Bambu Lab PLA Sparkle [19], as they contain reflective particles (photons) fused inside and external surface finish. Additionally, we chose Bambu Lab Silk [18] and Mika3D Silver Shiny PLA [21] as they blend reflective metal powder into their PLA polymer bases. The Bambu Lab PET-CF [17], which is carbon fiber reinforced PET (polyethylene terephthalate), is used as a comparison, since it is known as absorbing lights [31].

7.4.1 Sample production & Experiment Procedure. Using a Bambu Lab P1P 3D printer, we 3D printed $5 \times 5\text{cm}$ panels with a 5mm

thickness from elected filaments in Figure 26 a-f. The standard PLA settings were applied: 210°C printing temperature, 0.2mm layer height, 15% infill, and 220mm/s speed.

The panels were tested in a dark room under controlled lighting conditions: dim light (100lum), office light (500lum), and direct sunlight (1000lum) [1, 38], with illumination calibrated using Light Meter LM-3000 [13]. Light intensity reflected from the panels was measured five times per sample using our custom mobile application, *LightIntensity*, which captures surface reflectance in cd/m^2 . As shown in Figure 26m and Table 2, Bambu Lab PLA Silk filament [18] demonstrated the highest reflectivity.

7.4.2 Reflective Filament in Varying Color Space. As known from color theory, reflectivity varies by wavelength: white reflects most visible light, while darker colors like black absorb more, reducing reflected light intensity. We further evaluated the effect of seven color options of Bambu Lab PLA Silk filament [18]: white (#FFFFFF), silver (#EAECEB), pink (#EEB1C1), green (#4CE4A0), gold (#E5B03D), blue (#147BD1), and purple (#854CE4) as shown in Figure 26 f-l. Figure 26 n and Table 2 indicate the ranking from highest reflectivity to lowest reflectivity is: white > silver > pink > green > blue > gold > purple.

In sum, we confirm that the Bambu Lab PLA Silk filaments, particularly in white, silver, and pink, present the best reflection. However, our technique can be applied to reflective filaments of any brand and colors, though sensing efficiency may vary.

7.4.3 Modular Assembly for Reconfiguration. Snap-fit mechanisms are widely used for their assembly, disassembly, and reusability [46]. Such mechanisms use two flexible components designed with precise geometry and elasticity, allowing them to connect securely without additional hardware or adhesive. Our work has adapted several snap-fit designs (Figure 27) to ensure flexibility and compatibility with the physical constraints of various objects.

8 Validation & Evaluation

8.1 Light Intensity Optimization through Geometry Modification

We conducted a light intensity test on 3D printed panels that optimized surface light reflection using our technique with various colors of Bambu Lab PLA Silk Filaments [18]. The test followed the same procedure described in the filament selection light intensity test (Section 7.4). The objectives of this test are: (1) to demonstrate that our technique effectively optimizes light reflection across different color spaces, and (2) to explore whether color variations affect the light intensity received from panels made with our technique. As shown in Figure 28 (left), panels printed with our technique generally show higher light intensity compared to those without it. Figure 28 (right) and Table 3 present the reflectivity ranking from highest to lowest: white > pink > silver > green > gold > purple > blue. While this ranking differs slightly from the result of samples printed without our technique, the top three most reflective colors remain consistent. This slight variation in reflectivity ranking might be due to the interaction between the round and smooth geometry and the light. The semicircle infill lines create more surface area and angles for light to reflect from, but colors like blue, which

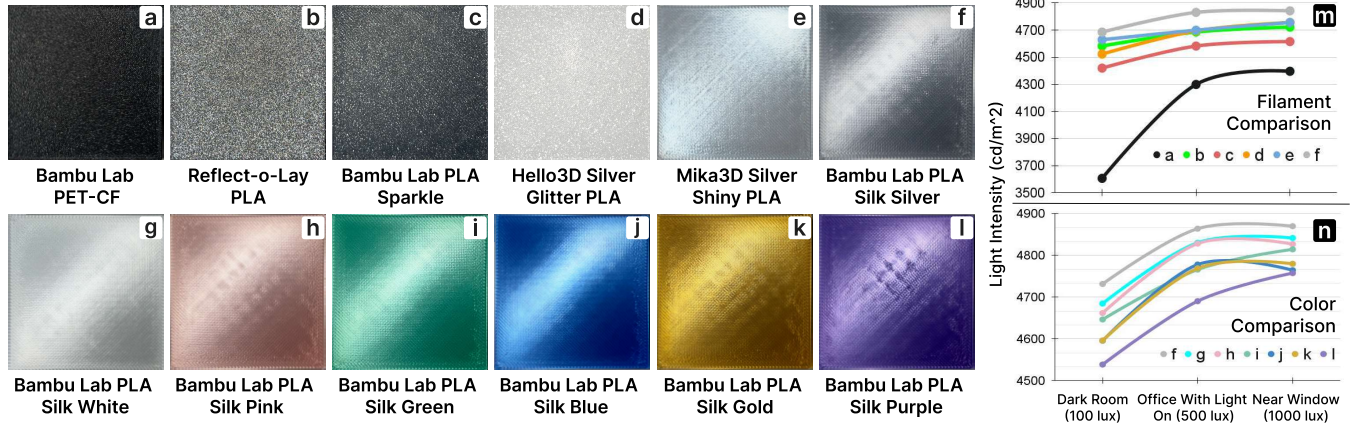


Figure 26: Printed samples of one light-absorbing filament, (a) Bambu Lab PEG-CF [17], and eleven reflective materials: (b) Reflect-o-Lay PLA [20], (c) Bambu Lab PLA Sparkle [19], (d) Hello3D Silver Glitter PLA [35], (e) Mika3D Silver Shiny PLA [21], Bambu Lab’s PLA Silk in (f) Silver [18], (g) White, (h) Pink, (i) Green, (j) Blue, (k) Gold, and (l) Purple. Two light intensity tests are conducted under three lighting conditions. Test 1 compares filaments from (a) to (g), with results shown in plot (m), indicating that Bambu Lab Silk filament has the best performance. Test 2 is followed to compare different colors of Bambu Lab Silk from (g) to (l), with results shown in plot(n).

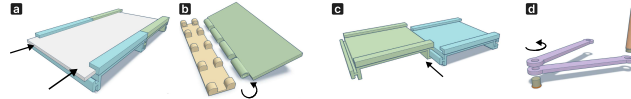


Figure 27: Selective examples of snap-fit mechanisms for modular assembly of markers: (a) sliding rail for long linear detection, (b) hinge for tilting and rotation detection, (c) marker area extensions, and (d) bar linkage.

typically absorbs more light, show lower reflectivity when the light is diffused across the curved surface.

8.2 Barcode Reading

We 3D printed ten EAN-13 standard barcodes using our technique, each embedding 95 bits of binary information. The bit size was set to 1mm width by 20mm height, consistent with the example shown in Section 5.1. One barcode contained test code, while the remaining nine embedded everyday commercial product information (Figure 29). Based on prior light intensity tests, we used three highly reflected filament colors—white, silver, and pink—with each color printing three barcodes.

All ten barcodes were successfully scanned using a commercial scanner app at varying distances and angles. Our custom decoding algorithm successfully scanned eight out of ten barcodes (details in Appendix C). Results suggest that brighter environments lead to higher recognition accuracy. At 1000lux, the barcode was accurately recognized at all angles except for 30°. For optimal performance, we recommend scanning from a distance of 10cm to 40cm (best results at 40cm) with an angle as close to perpendicular to the barcode as possible.

8.3 Dynamic Angle Sensing

We experimented to assess the accuracy of detecting rotating and tilting angles based on the reflective area’s position and geometric characteristics (i.e., a perfect circle). Using the spherical coordinate system, we tested the algorithm across various ϕ and θ angles of a tilting plate (Figure 20b), focusing only on ϕ due to its relevance to our sensing principle.

In this experiment, we set four θ angles, ranging from 10° to 40° in 10° increments (Figure 30a left). For each θ angle, we measured ϕ across a 360° range at 30° intervals (Figure 30a right). Results in Figure 30b-c indicate that as the tilting angle (θ) increases, the reflective sectors become more prominent, improving regression performance. The overall regression error was modest, demonstrating the promise of our proposed sensing mechanism.

9 Limitations, Discussion

Dimensional Limitation. Our geometry modification, achieved through Gcode computation, is sensitive to the 3D printer’s precision. If the nozzle size is too large or the stepper motor feeding the filaments does not support a proper resolution, our modified geometry can be applied to larger surfaces. Also, as our technique modifies Gcode for the top cover in the traditional layer-by-layer FDM process, which operates within 3 degrees of freedom, changing raster angles of surface fill lines outside of the XY-plane is not feasible. This motivated the development of modular assembly blocks to enable wrapping thin markers around complex bodies. However, systems offering more degrees of freedom, where the nozzle or print bed can be oriented around any surface normal (e.g., [11]), have the potential to extend the applicability of our techniques.

In addition, printing on top of non-flat surfaces starts with identifying fairly flat surfaces [3] to position the marker and then modifying the Gcode to allow nozzle strokes along the tangent planes.

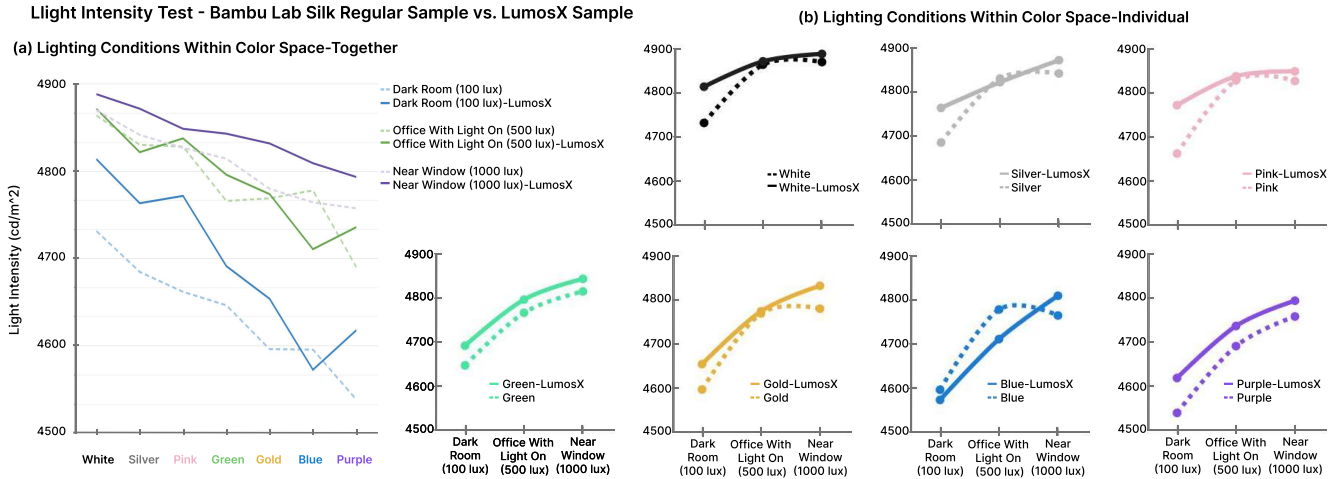


Figure 28: Comparison of the average light intensity measured from samples printed with and without the LumosX technique using seven colors of Bambu Lab PLA Silk filament [18] in Silver, White, Pink, Green, Blue, Gold, and Purple, under three lighting conditions. We show a comparison for each color together (a) and individually (b).



Figure 29: Ten 3D-printed EAN-13 barcodes embedding commercial product information. All ten barcodes were successfully scanned using a commercially available scanner, while eight out of ten were successfully scanned using our decoding algorithm.

For more complex surfaces such as the back of Stanford Bunny, the marker layer on the top of the target surface is distributed across multiple printing layers (Figure 31), making it challenging to define a group of coordinates for a single unit area. Our ongoing work focuses on investigating complex geometry processing to compute varying tangent slopes within one unit area. We plan to obtain the surface geometry of existing physical objects from repositories and 3rd parties, patching markers directly on top, as future work.

Advanced Sensing. Our exploration has shown the potential of 3D printed anisotropic reflection for interactive sensing by providing avenues to encode and decode binary digits of alternating 0 and 1. *LightIntensity* employing a regular RGB camera has demonstrated a proof of concept in detecting light patterns on the 3D-printed

units with low-cost computing resources available in any inexpensive smartphone. The immediate future work to investigate a sensing pipeline is facilitating higher bit-rate data transfer between our passive sensing units and cameras.

Sensitivity to Lighting and Angles. Tags based on brightness contrast, such as barcodes, are highly sensitive to both lighting conditions and viewing angles. If the ambient light is too dim or too bright, the contrast between binary 1 and 0 can become unclear, leading to decoding inaccuracies. Additionally, due to the nature of anisotropic reflection, the tag's appearance changes with the viewing angle. Depending on the light source and its position, areas designed to appear bright may instead look dark from certain angles, which also leads to potential decoding inaccuracies. We plan a comprehensive study to investigate how light source types, their

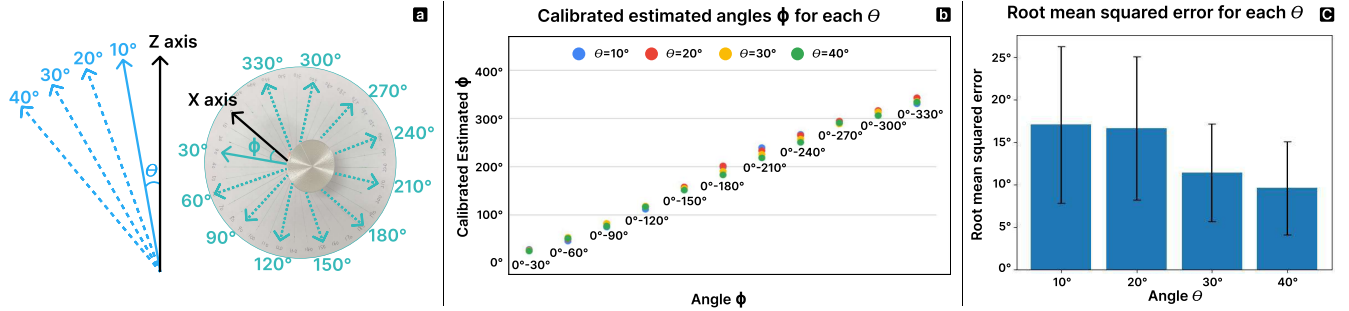


Figure 30: Results of angle sensing test. The ϕ angle ($0^\circ - 360^\circ$) is sensed at four different θ angles: 10° , 20° , 30° , and 40° (a). A comparison between the calibrated estimated ϕ and the actual ϕ is shown (b), and the root mean squared error is plotted (c).

intensity, distance, position, and perspective views affect decoding accuracy, identifying the optimal conditions for achieving the most stable and accurate results.

Acknowledgments

We thank our user study participants. This work is supported by the National Science Foundation (NSF) under award numbers IIS-2340120, IIS-2213842, and IIS-2213843.

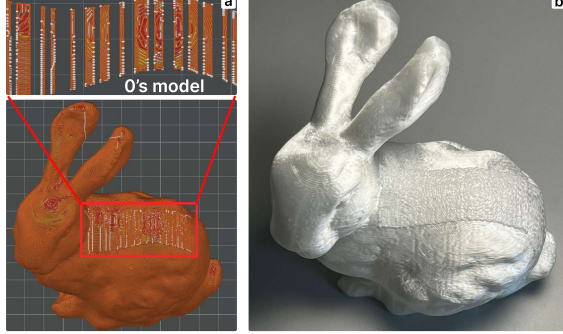


Figure 31: A Stanford Bunny with barcode (1's and 0's) on the top layer. The barcode model shows non-straight lines, indicating that raster angles are not preserved during slicing (a), resulting in a rough texture-reducing reflection (b).

10 Conclusion

Light carries rich information for users to make informed decision making through visual cues. In this work, we introduced LumosX, a new 3D-printed technique that employs anisotropic reflection—a ubiquitous light transfer phenomenon that varies with viewing angles. LumosX enables information encoding and decoding on 3D-printed real-world surfaces by optimizing directional reflection and brightness contrasts. This is achieved through precise control over processing parameters (e.g., raster angles, layer height, and extrusion amount) and the use of readily available light-reflective materials for low-cost FDM 3D printing. Our design also highlights composability through modular assembly, allowing for flexible re-encoding of information per application context. We validated our designs through rich indoor and smart urban sensing applications, facilitating people’s interaction and autonomous machine perception.

References

- [1] Shashank Kishore Bhandary, Rohit Dhakal, Vishwa Sanghavi, and Pavan Kumar Verkiculara. 2021. Ambient light level varies with different locations and environmental conditions: Potential to impact myopia. *PLOS ONE* 16, 7 (07 2021), 1–13. doi:10.1371/journal.pone.0254027
- [2] Douglas Chai and Florian Hock. 2005. Locating and decoding EAN-13 barcodes from images captured by digital cameras. In *2005 5th International Conference on Information Communications & Signal Processing*. IEEE, 1595–1599. doi:10.1109/ICICS.2005.1689328
- [3] Xiang ‘Anthony’ Chen, Stelian Coros, Jennifer Mankoff, and Scott E. Hudson. 2015. Encore: 3D Printed Augmentation of Everyday Objects with Printed-Over, Affixed and Interlocked Attachments. In *Proceedings of the 28th Annual ACM Symposium on User Interface Software & Technology* (Charlotte, NC, USA) (*UIST ’15*). Association for Computing Machinery, New York, NY, USA, 73–82. doi:10.1145/2807442.2807498
- [4] Arnaud Delmotte, Kenichiro Tanaka, Hiroyuki Kubo, Takuuya Funatomi, and Yasuhiro Mukaiyawa. 2020. Blind Watermarking for 3-D Printed Objects by Locally Modifying Layer Thickness. *IEEE Transactions on Multimedia* 22, 11 (2020), 2780–2791. doi:10.1109/TMM.2019.2962306
- [5] Mustafa Doga Dogan, Faraz Faruqi, Andrew Day Churchill, Kenneth Friedman, Leon Cheng, Sriram Subramanian, and Stefanie Mueller. 2020. G-ID: Identifying 3D Prints Using Slicing Parameters. In *Proceedings of the 2020 CHI Conference on Human Factors in Computing Systems* (Honolulu, HI, USA) (*CHI ’20*). Association for Computing Machinery, New York, NY, USA, 1–13. doi:10.1145/3313831.3376202
- [6] Mustafa Doga Dogan, Raul Garcia-Martin, Patrick William Haertel, Jamison John O’Keefe, Ahmad Taka, Akarsh Aurora, Raul Sanchez-Reillo, and Stefanie Mueller. 2023. BrightMarker: 3D Printed Fluorescent Markers for Object Tracking. In *Proceedings of the 36th Annual ACM Symposium on User Interface Software and Technology* (San Francisco, CA, USA) (*UIST ’23*). Association for Computing Machinery, New York, NY, USA, Article 55, 13 pages. doi:10.1145/3586183.3606758
- [7] Mustafa Doga Dogan, Ahmad Taka, Michael Lu, Yunyi Zhu, Aksht Kumar, Aakar Gupta, and Stefanie Mueller. 2022. InfraredTags: Embedding Invisible AR Markers and Barcodes Using Low-Cost, Infrared-Based 3D Printing and Imaging Tools. In *Proceedings of the 2022 CHI Conference on Human Factors in Computing Systems*. 1–12. doi:10.1145/3491102.3501951
- [8] Anil Eren and Hatice Dogan. 2022. Design and implementation of a cost effective vacuum cleaner robot. *Turkish Journal of Engineering* 6, 2 (apr 2022), 166+. doi:10.31127/tuje.830282
- [9] Jiří Filip. 2015. Analyzing and predicting anisotropic effects of BRDFs. In *Proceedings of the ACM SIGGRAPH Symposium on Applied Perception* (Tübingen, Germany) (*SAP ’15*). Association for Computing Machinery, New York, NY, USA, 25–32. doi:10.1145/2804408.2804419
- [10] Jiří Filip, Martina Kolářová, and Radomír Vávra. 2019. A Psychophysical Analysis of Fabricated Anisotropic Appearance. In *Pacific Graphics Short Papers*, Jehee Lee, Christian Theobalt, and Gordon Wetzstein (Eds.). The Eurographics Association. doi:10.2312/pg.20191333
- [11] Yisong Gao, Lifang Wu, Dong-Ming Yan, and Liangliang Nan. 2019. Near support-free multi-directional 3D printing via global-optimal decomposition. *Graphical*

- Models* 104 (2019), 101034. doi:10.1016/j.gmod.2019.101034
- [12] Cesar R Garcia, Jesus Correa, David Espalin, Jay H Barton, Raymond C Rumpf, Ryan Wicker, and Virgilio Gonzalez. 2012. 3D printing of anisotropic metamaterials. *Progress in Electromagnetics Research Letters* 34 (2012), 75–82. doi:10.2528/PIERL12070311
- [13] Lightray Innovation GmbH. 2023. Light Meter LM-3000. Available on the Apple App Store. <https://lightray.io/lightmeter/> Accessed 28 March 2024.
- [14] Ollie Hanton, Michael Wessely, Stefanie Mueller, Mike Fraser, and Anne Roudaut. 2020. ProtoSpray: Combining 3D printing and spraying to create interactive displays with arbitrary shapes. In *Proceedings of the 2020 CHI Conference on Human Factors in Computing Systems*. 1–13. doi:10.1145/3313831.3376543
- [15] Chris Harrison, Robert Xiao, and Scott Hudson. 2012. Acoustic barcodes: passive, durable and inexpensive notched identification tags. In *Proceedings of the 25th Annual ACM Symposium on User Interface Software and Technology* (Cambridge, Massachusetts, USA) (UIST '12). Association for Computing Machinery, New York, NY, USA, 563–568. doi:10.1145/2380116.2380187
- [16] Jong-Uk Hou, Do-Gon Kim, and Heung-Kyu Lee. 2017. Blind 3D Mesh Watermarking for 3D Printed Model by Analyzing Layering Artifact. *IEEE Transactions on Information Forensics and Security* 12, 11 (2017), 2712–2725. doi:10.1109/TIFS.2017.2718482
- [17] Bambu Lab Inc. 2023. Bambu Lab PEG-CF. <https://us.store.bambulab.com/products/pet-cf>
- [18] Bambu Lab Inc. 2023. Bambu Lab PLA Silk. <https://us.store.bambulab.com/collections/bambu-lab-3d-printer-filament/products/pla-silk-upgrade>
- [19] Bambu Lab Inc. 2023. Bambu Lab PLA Sparkle. <https://us.store.bambulab.com/collections/bambu-lab-3d-printer-filament/products/pla-sparkle>
- [20] Lay Filaments Inc. 2016. Reflect-o-Lay. <https://filament2print.com/gb/special-pla/690-reflect-o-lay.html>
- [21] MIKA3D Inc. 2022. MIKA3D Silk Metallic Silver Shiny PLA. <https://a.co/d/7snmEUH>
- [22] DV Isakov, Q Lei, F Castles, CJ Stevens, CRM Grovenor, and PS Grant. 2016. 3D printed anisotropic dielectric composites with meta-material features. *Materials & Design* 93 (2016), 423–430. doi:10.1016/j.matdes.2015.12.176
- [23] Yuhua Jin, Isabel Qamar, Michael Wessely, and Stefanie Mueller. 2020. Photochromelone Re-programmable multi-color textures using photochromic dyes. In *ACM SIGGRAPH 2020 Emerging Technologies*. 1–2. doi:10.1145/3332165.3347905
- [24] Konstantin Klamka and Raimund Dachselt. 2017. IllumiPaper: Illuminated Interactive Paper. In *Proceedings of the 2017 CHI Conference on Human Factors in Computing Systems*. 5605–5618. doi:10.1145/3025453.3025252
- [25] Dingzeyu Li, David I. W. Levin, Wojciech Matusik, and Changxi Zheng. 2016. Acoustic voxels: computational optimization of modular acoustic filters. *ACM Trans. Graph.* 35, 4, Article 88 (jul 2016), 12 pages. doi:10.1145/2897824.2925960
- [26] Dingzeyu Li, Avinash S. Nair, Shree K. Nayar, and Changxi Zheng. 2017. AirCode: Unobtrusive Physical Tags for Digital Fabrication. In *Proceedings of the 30th Annual ACM Symposium on User Interface Software and Technology* (Québec City, QC, Canada) (UIST '17). Association for Computing Machinery, New York, NY, USA, 449–460. doi:10.1145/3126594.3126635
- [27] Rong Lu, Jan J. Koenderink, and Astrid M.L. Kappers. 2000. Specularities on Surfaces with Tangential Hairs or Grooves. *Computer Vision and Image Understanding* 78, 3 (2000), 320–335. doi:10.1006/cviu.2000.0841
- [28] Zehua Ma, Hang Zhou, and Weiming Zhang. 2023. AnisoTag: 3D Printed Tag on 2D Surface via Reflection Anisotropy. In *Proceedings of the 2023 CHI Conference on Human Factors in Computing Systems* (Hamburg, Germany) (CHI '23). Association for Computing Machinery, New York, NY, USA, Article 420, 15 pages. doi:10.1145/3544548.3581024
- [29] Henrique Teles Maia, Dingzeyu Li, Yuan Yang, and Changxi Zheng. 2019. Layer-Code: optical barcodes for 3D printed shapes. *ACM Trans. Graph.* 38, 4, Article 112 (jul 2019), 14 pages. doi:10.1145/3306346.3322960
- [30] Andrii Matvienko, Andreas Löcken, Abdallah El Ali, Wilko Heuten, and Susanne Boll. 2016. NaviLight: Investigating Ambient Light Displays for Turn-by-Turn Navigation in Cars. In *Proceedings of the 18th International Conference on Human-Computer Interaction with Mobile Devices and Services* (Florence, Italy) (MobileHCI '16). Association for Computing Machinery, New York, NY, USA, 283–294. doi:10.1145/2935334.2935359
- [31] Pradeep Kumar Mishra, D Shashi Kumar Kumar, T Jagadesh, and Kartikeya Shukla. 2023. Experimental investigation into flexural and impact behaviour of 3D printed PETG short carbon fibre composite under solar light irradiation. *Proceedings of the Institution of Mechanical Engineers, Part C: Journal of Mechanical Engineering Science* 237, 16 (2023), 3597–3607. doi:10.1177/09544062221149923
- [32] Thingiverse user mitchell_cj. 2018. UV glow clock - by mitchell-cj. <https://www.thingiverse.com/thing:2775280> (Accessed on 2/9/2023).
- [33] Kongpyung (Justin) Moon, Jaeseong Yi, Valkyrie Savage, and Andrea Bianchi. 2024. 3D printed pyrography: Using wood filament and dynamic control of nozzle temperature for embedding shades of color in objects. *Additive Manufacturing* 83 (2024), 104064. doi:10.1016/j.addma.2024.104064
- [34] Parinya Punpongsanon, Xin Wen, David S. Kim, and Stefanie Mueller. 2018. *ColorMod: Recoloring 3D Printed Objects Using Photochromic Inks*. Association for Computing Machinery, New York, NY, USA, 1–12. <https://doi.org/10.1145/3173574.3173787>
- [35] LTD. SHENZHEN HELLO 3D TECHNOLOGY CO. 2018. HELLO3D Silver Glitter PLA. <https://a.co/d/4fc4beF>
- [36] Thingiverse user Swichmad. 2021. To avoid injury sign - slimmed by Swichmad. <https://www.thingiverse.com/thing:4794495> (Accessed on 2/9/2023).
- [37] Haruki Takahashi and Homei Miyashita. 2017. Expressive Fused Deposition Modeling by Controlling Extruder Height and Extrusion Amount. In *Proceedings of the 2017 CHI Conference on Human Factors in Computing Systems* (Denver, Colorado, USA) (CHI '17). Association for Computing Machinery, New York, NY, USA, 5065–5074. doi:10.1145/3025453.3025933
- [38] The Engineering ToolBox. 2004. Illuminance - Recommended Light Levels. https://www.engineeringtoolbox.com/light-level-rooms-d_708.html Accessed 29 March 2024.
- [39] Cesar Torres, Jasper O' Leary, Molly Nicholas, and Eric Paulos. 2017. Illumination aesthetics: Light as a creative material within computational design. In *Proceedings of the 2017 CHI Conference on Human Factors in Computing Systems* (CHI '17). Association for Computing Machinery, New York, NY, USA, 6111–6122. <https://doi.org/10.1145/3025453.3025466>
- [40] Hung-Yu Tseng, Rong-Hao Liang, Liwei Chan, and Bing-Yu Chen. 2015. LEaD: Utilizing Light Movement as Peripheral Visual Guidance for Scooter Navigation. In *Proceedings of the 17th International Conference on Human-Computer Interaction with Mobile Devices and Services* (Copenhagen, Denmark) (MobileHCI '15). Association for Computing Machinery, New York, NY, USA, 323–326. doi:10.1145/2785830.2785831
- [41] Thingiverse user west3dp. 2017. Good morning / good night glow in the dark 3D sculpture by west3dp. <https://www.thingiverse.com/thing:2518599> (Accessed on 2/9/2023).
- [42] Karl Willis, Eric Brockmeyer, Scott Hudson, and Ivan Poupyrev. 2012. *Printed Optics: 3D Printing of Embedded Optical Elements for Interactive Devices*. Association for Computing Machinery, New York, NY, USA, 589–598. <https://doi.org/10.1145/2380116.2380190>
- [43] Karl D. D. Willis and Andrew D. Wilson. 2013. InfraStructs: fabricating information inside physical objects for imaging in the terahertz region. *ACM Trans. Graph.* 32, 4, Article 138 (Jul 2013), 10 pages. doi:10.1145/2461912.2461936
- [44] Fei Yan, Mark Eilers, Martin Baumann, and Andreas Luedtke. 2016. Development of a lane change assistance system adapting to driver's uncertainty during decision-making. In *Adjunct Proceedings of the 8th International Conference on Automotive User Interfaces and Interactive Vehicular Applications*. 93–98. doi:10.1145/3004323.3004334
- [45] Xiaoying Yang, Jacob Sayono, and Yang Zhang. 2023. CubeSense++: Smart Environment Sensing with Interaction-Powered Corner Reflector Mechanisms. In *Proceedings of the 36th Annual ACM Symposium on User Interface Software and Technology*. 1–12. doi:10.1145/3586183.3606744
- [46] Keisuke Yoshida and Hirofumi Wada. 2020. Mechanics of a Snap Fit. *Phys. Rev. Lett.* 125 (Nov 2020), Issue 19. doi:10.1103/PhysRevLett.125.194301
- [47] Jianqi Zeng, Honghao Deng, Yunyi Zhu, Michael Wessely, Axel Kilian, and Stefanie Mueller. 2021. Lenticular Objects: 3D Printed Objects with Lenticular Lens Surfaces That Can Change their Appearance Depending on the Viewpoint. In *The 34th Annual ACM Symposium on User Interface Software and Technology* (Virtual Event, USA) (UIST '21). Association for Computing Machinery, New York, NY, USA, 1184–1196. doi:10.1145/3472749.3474815
- [48] Yang Zhang, Sven Mayer, Jesse T. Gonzalez, and Chris Harrison. 2021. Vibrosight++: City-Scale Sensing Using Existing Retroreflective Signs and Markers. In *Proceedings of the 2021 CHI Conference on Human Factors in Computing Systems* (Yokohama, Japan) (CHI '21). Association for Computing Machinery, New York, NY, USA, Article 410, 14 pages. doi:10.1145/3411764.3445050

A Computation to Maximize Reflection Area

Informed by the prior work [37], the volume of filament fed (V_f) should be equivalent to the volume of filament extruded (V_i). Let S_f and l_f be the cross-section area (mm^2) and length (mm) of the fed filament, and S_i and l_i be the cross-section area (mm^2) and length (mm) of the printed infill line. An object's volume is calculated by multiplying its cross-section area by its length, and we have:

$$S_f * l_f = S_i * l_i \quad (2)$$

To compute S_f , simply use the equation to compute the surface area of a circle, whose radius is given by the half of filament diameter d_f known from the manufacturer:

$$S_f = \pi \left(\frac{d_f}{2} \right)^2 \quad (3)$$

To compute S_i , one needs to define the desired geometry of optimized infill lines. In this work, we follow a prior work [28] which designs the infill line to be half-cylinder, so the cross section is a semicircle. The semicircle height is equivalent to the desired height of the half-cylinder (h_c). The width of the semicircle is controlled by the line width (w) that we set in printing settings (we use the default value of $0.4mm$ in this case), so S_i is defined by:

$$S_i = \frac{1}{2} \pi h_c \frac{w}{2} \quad (4)$$

Substituting Eq. 3 and Eq. 4 in Eq. 2 we can get:

$$\pi \left(\frac{d_f}{2} \right)^2 l_f = \frac{1}{2} \pi h_c \left(\frac{w}{2} \right) l_i \quad (5)$$

Rearranging Eq. 5 yields the formula to calculate the length of filament to be fed:

$$l_f = \frac{h_c w}{(d_f)^2} l_i \quad (6)$$

Prior work suggests preventing compression and preserving the surface tension of the printed half-cylinder-shaped line [28], thus we adjusted the obtained fed filament length into the nozzle l_f by a specific coefficient c to compute the final value of E :

$$E = c \times l_f \quad (7)$$

This coefficient is typically less than 1, and we used 0.85.

As an example, the top surface of a $5cm$ by $5cm$ panel to be printed has several $1cm$ by $5cm$ unit areas with either 90° (vertical) or 0° (horizontal) raster angles as shown in Figure 24a. One printed line in the horizontal unit area has a fixed line length of $1cm$ (l_i). Let the desired half-cylinder be $0.2mm$ high (h_c) and the line width be the same as the nozzle size, $0.4mm$ (w). The diameter of the filament is given as $1.75mm$ (d_f). Substituting all the values in Eq. 6 and plugging computed l_f into Eq. 7 with the coefficient $c = 0.85$,

$$E = 0.85 \times \left(\frac{0.2 \times 0.4}{1.75^2} \times 10 \right) \approx 0.22204.$$

To compute the E value for the vertical unit area, doing the same with $l_i = 50$ will result in $E \approx 1.11020$. According to the prior work [28], we hard cut at 5 decimals.

For accurate computation within the slicer software, it is crucial to activate the “M83 relative extrusion mode”, as it allows for the adjustment of the extrusion amount of each line independently,

without being impacted by previous extrusion or impacting others following. Additionally, several parameters can be adjusted including the line width w (mm), layer height (mm), infill density (percentage), printing speed (mm/s), and printing position. We adopted a $0.4mm$ line width matching the nozzle diameter, but variations in width depending on the choice of nozzle size are also feasible. We recommend setting the layer height to $0.2mm$, which is half the nozzle diameter, and 100% infill to ensure structural rigidity. Empirically, a printing speed between $20mm/s$ to $50mm/s$ is advised for optimal surface smoothness.

B Light Intensity Test

Table 2 and Table 3 contain data of the two light intensity tests.

C Experiment Setup for Custom Algorithm Based Barcode Testing

To further investigate factors that could impact sensing performance, we conducted a barcode recognition study with two variables: *illumination intensity* and *camera angle*. Printed barcodes were attached to a flat black foam board, and angles ranging from 30° to 90° were measured in 15° increments using a protractor. Input images of the barcodes were taken using an iPhone 12 mini from a $50cm$ distance.

To vary illumination, an LED lamp was adjusted to achieve 100 , 500 , and $1,000lux$, measured using the Light Meter LM-3000 app [13]. We captured a photo for each combination of luminance and angle, resulting in a total of 15 inputs. The barcode was accurately recognized at all angles except for 30° , in which two digits in the middle were misread.

D Experiment Setup for Dynamic Angle Sensing

We conducted the evaluation by setting θ angles at 10° , 20° , 30° , and 40° . For each θ , ϕ angles were tested at 12 positions spanning a full 360° range with 30° intervals (Figure 30a right). A total of 48 images (4×12 configurations) were captured using an iPhone 12 mini with the flash on. The tilting panel algorithm from Section 6.4 was applied to evaluate the decoding of angle information. Calibration used $\phi = 0$ as a reference point, adjusting other ϕ values by subtracting offsets.

Figure 30b shows a comparison between the calibrated estimated ϕ angles and ground truth values for each θ . Figure 30c plots the root mean squared error (RMSE) for each configuration. Larger tilting angles (θ) improved regression performance due to the increased prominence of reflective sectors.

E Preliminary User Study Findings

To validate the user's perception and engagement with our applications and gather insights on the engagement with our technique, we conducted a study with 7 participants ($N=7$, Female=3, Male=4, ages ranged 18–34). Participants were shown 10 real-world scenarios, varying from pet feeder to car parking assistance, and interacted directly with 3D-printed LumosX applications. They rated their experience on a 1–5 Likert scale, focusing on (1) decoded signals' readability (perception), (2) real-life applicability (practicality), and (3) integration with the ambient environment (obtrusiveness). Figure 32 summarizes these results. Participants also shared qualitative

Filament Type	Measured Light Intensity (cd/m ²)																	
	Dark Room (100 lux)					Average	Office With Light On (500 lux)					Near Window (1000 lux)						
1	2	3	4	5	Average	1	2	3	4	5	Average	1	2	3	4	5	Average	
Bambu Lab PEG-CF	3600	3613	3600	3612	3608	3606.60	4295	4298	4304	4295	4302	4298.8	4395	4395	4391	4391	4408	4396
Reflect-o-Lay PLA	4587	4588	4580	4580	4578	4582.6	4686	4691	4691	4678	4683	4685.8	4721	4717	4721	4725	4725	4721.8
Bambu Lab PLA Sparkle	4429	4417	4417	4417	4417	4419.4	4582	4581	4580	4585	4582	4582	4613	4617	4616	4613	4616	4615
Hello3D Silver Glitter PLA	4522	4525	4525	4525	4518	4523	4696	4698	4693	4691	4693	4694.2	4757	4752	4755	4752	4763	4755.8
Mika3D Silver Shiny PLA	4629	4632	4626	4629	4627	4628.6	4698	4698	4700	4698	4700	4698.8	4757	4757	4751	4761	4752	4755.6
Bambu Lab PLA Silk Silver	4688	4681	4686	4688	4681	4684.8	4831	4829	4831	4831	4831	4830.2	4845	4845	4840	4838	4840	4841.6
Bambu Lab PLA Silk White	4728	4732	4738	4732	4728	4731.6	4866	4863	4864	4863	4863	4863.8	4869	4872	4869	4868	4871	4869.8
Bambu Lab PLA Silk Pink	4663	4663	4658	4663	4663	4662	4831	4828	4827	4828	4827	4828.2	4827	4826	4829	4825	4827	4826.8
Bambu Lab PLA Silk Green	4645	4647	4647	4647	4647	4646.6	4765	4769	4765	4764	4767	4766	4815	4813	4816	4813	4815	4814.4
Bambu Lab PLA Silk Gold	4604	4591	4591	4605	4591	4596.4	4768	4768	4763	4772	4774	4769	4779	4785	4776	4778	4781	4779.8
Bambu Lab PLA Silk Blue	4591	4601	4591	4598	4598	4595.8	4781	4778	4776	4774	4781	4778	4763	4774	4763	4761	4761	4764.4
Bambu Lab PLA Silk Purple	4536	4536	4543	4543	4536	4538.8	4691	4693	4691	4691	4686	4690.4	4757	4761	4757	4752	4761	4757.6

Table 2: Measured light intensity of panels printed with twelve reflective filaments.

Filament Type	Measured Light Intensity (cd/m ²)																	
	Dark Room (100 lux)					Average	Office With Light On (500 lux)					Near Window (1000 lux)						
1	2	3	4	5	Average	1	2	3	4	5	Average	1	2	3	4	5	Average	
Bambu Lab PLA Silk Silver	4765	4760	4761	4763	4768	4763.4	4820	4825	4825	4818	4821	4821.8	4876	4872	4870	4870	4870	4871.6
Bambu Lab PLA Silk White	4813	4814	4812	4816	4814	4813.8	4871	4870	4871	4875	4870	4871.4	4890	4886	4889	4887	4889	4888.2
Bambu Lab PLA Silk Pink	4771	4774	4768	4774	4772	4771.8	4836	4839	4838	4840	4835	4837.6	4846	4845	4850	4850	4852	4848.6
Bambu Lab PLA Silk Green	4691	4688	4691	4696	4691	4691.4	4792	4795	4798	4795	4800	4796	4843	4842	4844	4842	4844	4843
Bambu Lab PLA Silk Gold	4657	4652	4654	4649	4658	4654	4773	4778	4772	4774	4772	4773.8	4834	4829	4831	4833	4832	4831.8
Bambu Lab PLA Silk Blue	4575	4570	4572	4572	4575	4572.8	4713	4712	4709	4710	4710	4710.8	4810	4810	4809	4808	4809	4809.2
Bambu Lab PLA Silk Purple	4616	4617	4616	4624	4617	4618	4732	4738	4734	4738	4738	4736	4798	4797	4793	4788	4791	4793.4

Table 3: Measured light intensity of panels printed with seven Bambu Lab PLA Silk filaments using the LumosX technique.

feedback on challenges, potential application contexts (integrated into Section 5), and suggestions for improvement.

E.0.1 Perception & Obtrusiveness. Overall, participants liked the applications and their potential use scenarios. They found most applications and scenarios easy to use and well-blended with the environment. "Nothing much challenging since I would [...] just reading the notification [of decoded signal]" (P1). A participant with a design background commented from aesthetic perspectives, "[it's blended well if] it's positioned near the bottom lip of the cup. (P3)".

E.0.2 Practicality & Use Cases. While P1 first saw checking the left amount in the container as unnecessary compared to the weight sensor, P4, and P5 showed gratitude for use cases involving the pet feeder. P1 appreciated the ability to track habits in the long-term, noting "a really good way to track pet habits". P4 valued precise portion tracking, noting that "[...] without the system, estimating the portions for me would be difficult to tell the granular changes from the camera directly, but this issue is solved with the system computing the difference". P5 emphasized the utility for pet owners traveling away from home: "this approach will be significantly helpful for [...] monitor[ing] their cat's health and well-being remotely".

Several participants also identified potential new use cases for the informative markers and barcodes. P2 identified additional potential for markers in accessibility assistance, particularly in the vacuum robot guide example: "I think this can also be applicable for improving accessibility [for indoor navigation by the visually impaired]". P2 proposed using them for electronics organization: "I would like to have it on my electronics boxes in the lab. So that I do not need to open and go through every component inside to find the one that I

am looking for." P4 envisioned applications in inventory tracking or child daycare management, stating, "[...It] would be cool to [use] in a camera system in a home that keeps track of where items were last seen [...] or maybe [as] a unique identifier/tracker for children in a daycare". P1 further expanded the parking assistance for the space availability checker if integrated into the central system, and P2 suggested the angle markers can also tell new drivers where to turn their steering wheels. P3 saw opportunities in industry applications, "I can see a more apt context in places [...] for large groups of varying individuals who might need their objects to be serviced in a particular way [...] in food service, fulfillment, or factories (essentially highly sequential, large groups of processes being serviced) using covert signals from proximity in the environment".

In addition, tangible controllers' flexibility was well received, "the coolest thing is it allows you to build your own controllers based on different actions. [...] clicking, but also sliders and knobs that allowed for other interactions (P4)".

E.0.3 Challenges. Many interesting improvements in application ideas have been discussed. "Measuring distances between two surfaces is important for machining, if there can be a non-destructive tool that would allow users to measure then this would be very useful. (P7)". The 3D printing experts shared concerns regarding maintenance as it "need to be durable and wear-tear resistant in case a car goes over it. (P1)" P1 also imagined how the occlusion of markers would be resolved, "what if children dropped toys or someone put down a box in a vacuum['s path]?" which left us future work, in addition to a tracking system that logs which set of markers the vacuum visited to keep track of the coverage (P4).

User Study Scenario List

Scenario 1. LumosX Barcode - jewelry plate & food containers
Scenario 2. LumosX Barcode - smart appliance
Scenario 3. Pet Feeder - low food level
Scenario 4. Pet Feeder - daily food consumption check
Scenario 5. Parking Assistant
Scenario 6. Bike Lane Assistant
Scenario 7. Tangible Controller
Scenario 8. Vacuum Robot Guide
Scenario 9. Room Brightness Control
Scenario 10. TV Position Adjustment

(1=Strongly Disagree, 5=Strongly Agree)

Scenario	1	2	3	4	5	Mean	Total Mean
Q1. I am confident that I can read the decoded signals.							
1		1		6		3.71	
2		1	1	3	2	3.86	
3				3	4	4.57	
4				3	4	4.57	
5			1	2	4	4.43	
6	1			4	2	4.00	
7			1	4	2	4.14	
8				4	3	4.43	
9	1			2	4	4.29	
10			1	4	2	4.14	

4.21

(1=Strongly Disagree, 5=Strongly Agree)

Scenario	1	2	3	4	5	Mean	Total Mean
Q2. I will use this application in real life. The information displayed is not obtrusive (not obvious), well blended with the [environment].							
1		2	2	2	1	3.29	
2	1	3	3			3.29	
3		1	5	1		4.00	
4			3	4		4.57	
5	1	1	4	1		3.71	
6	1	3	2	1		3.43	
7	1		3	3		4.14	
8		1	4	2		4.14	
9	1		2	4		4.29	
10		1	4	2		4.14	

(1=Strongly Disagree, 5=Strongly Agree)

Scenario	1	2	3	4	5	Mean	Total Mean
Q3. The information displayed is not obtrusive (not obvious), well blended with the [environment].							
1		1		3	3	4.14	
2			2	2	3	4.14	
3				4	3	4.43	
4				2	5	4.71	
5				3	4	4.57	
6				6	1	4.14	
7	1			4	2	4.00	
8				2	5	4.71	
9				3	4	4.57	
10				3	4	4.57	

4.40

Figure 32: Result of participants' ratings on ten real-world scenarios.